University Library



A gateway to Melbourne's research publications

Minerva Access is the Institutional Repository of The University of Melbourne

Author/s:
Liu, W;Tian, Y;Cassidy, MJ;O'Loughlin, C;Watson, P

Title:
Numerical Investigation of the Capacity of Anchor Chain Links in Clay

Date:
2024-10-01

Citation:
Liu, W., Tian, Y., Cassidy, M. J., O'Loughlin, C. & Watson, P. (2024). Numerical Investigation of the Capacity of Anchor Chain Links in Clay. Journal of Geotechnical and Geoenvironmental Engineering, 150 (10), https://doi.org/10.1061/JGGEFK.GTENG-11676.

Persistent Link:
https://hdl.handle.net/11343/354827

Manuscript
Click here to access/download;Manuscript;Manuscript-Clean version.docx

Numerical Investigation of the Capacity of Anchor Chain Links in Clay

Wenlong Liu
PhD student
Department of Infrastructure Engineering, Faculty of Engineering and Information Technology
The University of Melbourne, Parkville, Victoria 3010, Australia
Email: wenlong@student.unimelb.edu.au

Yinghui Tian (corresponding author)
ARC Future Fellow
Department of Infrastructure Engineering, Faculty of Engineering and Information Technology
The University of Melbourne, Parkville, Victoria 3010, Australia
Email: yinghui.tian@unimelb.edu.au

Mark J. Cassidy
Professor
Department of Infrastructure Engineering, Faculty of Engineering and Information Technology
The University of Melbourne, Parkville, Victoria 3010, Australia
Email: mark.cassidy@unimelb.edu.au

Conleth O'Loughlin
Professor
Centre for Offshore Foundation Systems and Oceans Graduate School
The University of Western Australia, 35 Stirling Highway, Crawley WA 6009, Australia
Email: conleth.oloughlin@uwa.edu.au

Phil Watson
Professor
Centre for Offshore Foundation Systems and Oceans Graduate School
The University of Western Australia, 35 Stirling Highway, Crawley WA 6009, Australia
Email: phillip.watson@uwa.edu.au

Submitted as Technical Paper
Words: ~5,900 (excluding references and acknowledgment)
Figures: 12
Tables: 1

Numerical Investigation of the Capacity of Anchor Chain Links in Clay

Abstract

Offshore floating systems are held in position with chains that connect the structure with anchors embedded in the seabed. An essential component to calculating the overall mooring capacity is an accurate assessment of holding resistance from the anchor chains. Existing studies have generally simplified the (complex) chain geometry to that of a cylindrical bar, which does not account for the intricate geometry of the connected chain links. This paper reports on three-dimensional finite element modelling that defines the capacity of a link of anchor chain in clay soil with consideration of the geometry of the chain links, including the influence from adjacent links. Both stud link and studless links are considered, along with the effect of embedment depth, link direction angle and interface condition, and explored across a comprehensive finite element analysis study. The soil resistance acting on the chain links, represented with uniaxial bearing capacity factors ($N_{n,\max}$, $N_{s,\max}$, and $N_{t,\max}$) along the normal, lateral and axial directions of the chain link respectively, are derived and the soil failure mechanisms for these conditions discussed. Equivalent bearing capacity factors, N_q and N_a are then derived by converting the soil resistance to normal and tangential resistances (q and f) acting on an equivalent cylindrical bar. Ultimately, f/q is calculated to represent the friction coefficient, μ, which ranges from 0.2 to 0.4.

Keywords

Anchor chain; bearing capacity; finite element modelling; soil resistance

1 Introduction

The demand for mooring systems that secure buoyant offshore facilities is increasing – as engineers push developments into deeper waters and with novel applications, such as floating wind turbines, wave energy converters and offshore fish farms. As a key component of the mooring system design, mooring lines connect the floating facility to an anchor point embedded in the seabed, and can have a catenary, taut, semi-taut or vertical tethering configuration. The segment of the mooring line embedded in and lying on the seabed plays an important role because (1) the frictional capacity along this segment can be a major component of the overall capacity (Neubecker and Randolph 1995), especially for catenary moorings; (2) the loading angle at the attachment point of the anchors affects the performance of the embedded anchor (Supachawarote et al. 2004, O'Loughlin et al. 2017), substantially determining the ultimate embedment depth and holding capacity (Tian et al. 2015). The segment of mooring line embedded in the seafloor typically uses metallic chains due to the advantage of heavier weight (higher friction), less excursion (Yen and Tofani 1984) and better overall performance to avoid chafing when compared with wire or synthetic fibre rope.

Current engineering practice simplifies a mooring chain as an equivalent cylindrical bar, as reflected in design guidance (e.g. ABS 2017, DNV 2017), and describes the soil resistance as a normal, q, and a tangential component, f, per unit length of chain:

$$q = E_n d N_c s_u \tag{1}$$

$$f = E_t d \alpha_{soil} s_u \tag{2}$$

where E_n and E_t are multipliers on the bar diameter of the chain link, d, in the normal and tangential

79 directions, respectively; N_c is a bearing capacity factor; α_{soil} is the (interface) friction ratio and s_u is
80 the undrained shear strength. E_n and E_t are geometrical parameters that can be calculated directly
81 from the geometry of the chain links, although there is additional uncertainty associated with the
82 chain orientation (about its longitudinal axis) and whether soil passes through or becomes trapped in
83 the chain links. Design guidance (DNV 2017 and ABS 2017) is consistent on their recommendations
84 for the normal multiplier (E_n = 2.5), with slight variation on their recommendations for the range of
85 bearing capacity factor (N_c = 9 to 14 (DNV 2017) and N_c = 7.6 to 14.1 (ABS 2017)), and a larger
86 discrepancy on the selection of the tangential multiplier, E_t, with DNV (2017) recommending E_t =
87 11.3 and ABS (2017) suggesting the range, E_t = 8 to 11. DNV (2017) also provided a range of values
88 for the friction ratio, α_{soil} = 0.4 to 0.6.

89 Neubecker and Randolph (1995) proposed a closed-form analytical solution for the response of an
90 embedded anchor line, employing a friction coefficient, μ, defined as the ratio of tangential to normal
91 resistance, $\mu = f/q = E_t\alpha_{soil}/E_nN_c$. They analysed experimental data reported by Degenkamp and Dutta
92 (1989) to recommend that the friction coefficient should be in the range, μ =0.27 to 0.69. A more
93 recent experimental study by Han and Liu (2017) showed that the friction coefficient varied as the
94 inverse catenary formed, but stabilised at μ = 0.3, within the range recommended by Neubecker and
95 Randolph (1995). Rocha et al. (2016) reported data from model scale experiments and back analysed
96 the data to infer the friction coefficient in the range, μ = 0.16 to 0.61, which is also similar to the
97 range reported in Neubecker and Randolph (1995), but still extremely varied for application in
98 offshore conditions. As also noted by Frankenmolen et al. (2016), reported and recommended values
99 of the friction coefficient, μ, occupy a wide range, such that there is uncertainty regarding their
100 selection, which will also lead to uncertainty in the amount of mooring line load taken by the

101 embedded chain, and on the uplift angle at the anchor.

102 The uncertainty noted above provides the motivation for this study, which aims to deduce the soil
103 resistance acting on mooring chain links in a more rigorous manner. This is achieved through the use
104 of three-dimensional finite element modelling that considers the intricate chain link geometry of both
105 stud and studless chains, chain link embedment depth, interface condition and chain link direction
106 angle. Whilst the focus of this paper is on the resistance acting on individual chain links, the results
107 presented here form the basis for the analysis of a continuous embedded mooring chain, as described
108 in Liu et al. (2023).

109 **2 Three-dimensional finite element modelling**

110 Chain-soil analyses typically simplify the chain as an equivalent cylindrical bar, whereas actual chain-
111 soil interaction mechanisms are more complex due to the intricate geometry of the chain links. Fig. 1
112 shows the geometry of the so-called '6*d* chain' stud link and studless chains used offshore. The link
113 length, L, is 6d for both chain types (where d is the bar diameter as defined earlier), whereas the chain
114 link width, $W = 3.6d$ for the stud link chain and $W = 3.35d$ for the studless chain.

115 A 6d chain with a bar diameter of $d = 0.1$ m was considered in this study, where the link length is
116 $L = 0.6$ m and the width is $W = 0.36$ m and 0.335 m for the stud and studless link, respectively.
117 According to Vryhof Anchors (2015), the breaking load of stud and studless chains with Grade R5 is
118 11.5 MN. Considering the high yield stress of the steel chain and the stiffness of the link relative to
119 that of the soil, the links were modelled as rigid bodies in the finite element model, leading to
120 computational efficiency.

As shown in Fig. 2, the origin of the global coordinate system x-y-z is on the top surface of the soil domain, which had a length and height (in the y-z plane) of $14L$ to minimise potential boundary effects. Along the x direction, one whole link and two adjacent half links were considered in the finite element model, in order to obtain the soil resistance of a single chain link whilst accounting for the effect of adjacent links. The corresponding nodes on the front and back faces of the soil (along the x direction) were coupled using the MPC (multipoint constraints) technique (see Dassault Systèmes 2019 for technical details) to mimic a cyclic symmetric condition (i.e. a representative segment of an infinitely long chain). The lower boundary of the soil domain ($z = 14L$) was fixed and the top boundary ($z = 0$) was free, while the side boundaries ($y = \pm 7L$) were set as roller-supported (allowing vertical but not horizontal displacement).

The soil was modelled as an elastic perfectly plastic Tresca material to simulate the undrained behaviour of a clay seabed. A uniform undrained shear strength, $s_u = 50$ kPa was considered in the study, with the elastic behaviour of the soil modelled with a Young's Modulus, $E = 500 s_u$ and Poisson's Ratio, $v = 0.49$ (to ensure minimal volume change while maintaining numerical stability). It is noted that the uniform soil strength assumption was deemed adequate as the observed chain-soil mechanisms are limited to local failure modes. Furthermore, all the numerical results were normalised by s_u, allowing for broader application to seabeds with different soil strength profiles.

The middle chain link and two adjacent half links are treated as three independent rigid bodies, allowing the soil resistance associated with displacement of the middle link to be obtained from the results. The chain-soil interface does not allow separation in the normal direction, which is appropriate for undrained conditions in clay as suction at the trailing edge of the chain link is expected

to maintain contact between the chain and the soil. The maximum shear strength, τ_{max}, at the chain-soil interface is defined as αs_u, where interface roughness values, $\alpha = 0$, 0.2, 0.4, 0.6, 0.8, 1 and ∞ were considered in this study. $\alpha = 0$ represents a fully smooth interface, with no shear resistance along the interface. $0 < \alpha \leq 1$ represents an intermediate roughness, with $\alpha = 1$ giving the maximum shear resistance, $\tau_{max} = s_u$, which is commonly referred to as a 'rough' interface. $\alpha = \infty$ represents the condition where the chain-soil nodes are directly coupled together and no sliding is allowed (τ_{max} can be infinite); this is commonly referred to as a 'fully bonded' condition. In this study, $\alpha = \infty$ was technically realised by using the 'Tie' constraint (see Dassault Systèmes 2019) for the chain-soil interface (see Liu et al. 2021 for a detailed discussion).

A fine mesh (with a typical element size of ~ d/20) was used in the soil region close to the chain links, with a transition to a coarse mesh used elsewhere. A typical calculation case had ~140,000 hexahedral full integration elements, which was verified to achieve good accuracy with acceptable computation efficiency.

As shown in Fig. 2, the load and displacement of the middle chain link are denoted as N and w for the normal direction, S and u for the lateral direction, and T and v for the axial direction. The v axis is taken as perpendicular to the front and back planes coupled with MPC, and the middle chain link is orthogonal to two adjacent half links. The chain embedment depth, z, is measured as the distance between the soil surface and the centre of the middle link. For example, when $z = 0$ the centre of the chain link is at the soil surface. The chain link direction angle, β, is defined as the angle between the w axis of the middle chain link and the vertical plane x-z in the global coordinate system. As detailed in Table 1, embedment depths of $z/W = 0$, 0.64, 1, 1.5, 2, 2.5, 3 and 11 were considered, along with

direction angles of β = 0°, 15°, 30°, 45°, 60°, 75°, and 90° (see Fig. 2 for illustration of β = 0°, 15° and 90° at z = 0).

In total, the study involved 762 individual finite element analyses with different chain link types (stud and studless), embedment depths, direction angles and interface roughness, as detailed in Table 1. A typical case took approximately 20 minutes to run by using 13 CPU and 2 GPU cores, along with 39 GB memory, in a high-performance computing system - amounting to a total running time of 254 hours.

3 Normal, lateral and axial soil resistance to displacement of the chain links

Uniaxial soil resistances, N, S and T to movement of the middle chain link are obtained by displacing the chain and two adjacent half links together along the w, u and v axes, respectively. Results from all 762 analysis cases are detailed in Table 1, with selected results considered in more detail in the following sections. Results for a deeply embedded stud and studless link with a fully bonded chain-soil interface (z/W = 11, β = 0° and $\alpha = \infty$) are discussed initially in the following two sections, before considering the effect of embedment depth, chain link direction angle and interface roughness.

3.1 Stud link chain

Fig. 3 shows the soil resistance versus displacement for a deeply embedded stud link. As expected for an elastic-perfectly plastic response, the normal, lateral and axial soil resistances in Fig. 3 increase with displacement before stabilising at constant values. The stabilised normal, lateral and axial resistances are termed the uniaxial capacities, N_{max}, S_{max} and T_{max}. For the deeply embedded stud link with a fully bonded chain-soil interface case shown in Fig. 3, N_{max} = 87.8 kN, S_{max} = 47.0 kN and

T_{max} = 20.7 kN. The projected areas along the *w*, *u* and *v* axis, denoted as A_w, A_u and A_v, respectively, essentially correspond to the shaded zones in the plane of *u*-*v*, *w*-*v* and *u*-*w* as shown in Fig. 1. For the stud link in this study, A_w = 0.139 m^2, A_u = 0.058 m^2, and A_v = 0.034 m^2. Dimensionless bearing capacity factors can then be calculated as $N_{max}/A_w s_u$ = 12.64, $S_{max}/A_w s_u$ = 6.76 (or $S_{max}/A_u s_u$ = 16.21) and $T_{max}/A_w s_u$ = 2.98 (or $T_{max}/A_v s_u$ = 12.18). Considering the projected area along the *w* axis (*u*-*v* plane), A_w, for each resistance allows the relative magnitudes to be interpreted readily, whereas considering the projected area along the axis relevant to the direction of displacement allows for a comparison with the normal bearing capacity factor of a plate anchor, as discussed below.

As illustrated in Fig. 4, O'Neill et al. (2003) proposed upper bound solutions for capacity in the vertical (or normal) and lateral directions, V_{max} and H_{max}, respectively, for a deeply embedded rectangular plate anchor of length, L_f and thickness, d_f

$$\frac{V_{max}}{L_f s_u} = 4\left(\pi - \theta + \frac{\tan\theta}{2}\right) + 4\frac{d_f}{L_f}\left(\frac{1}{2} + \cos\theta\right) \tag{3}$$

$$\frac{H_{max}}{L_f s_u} = 4\frac{d_f}{L_f}\left(\pi - \theta + \frac{\tan\theta}{2}\right) + 4\left(\frac{1}{2} + \cos\theta\right) \tag{4}$$

By varying θ, the minimum values of Eqs. (3)~(4) are obtained as upper bound solutions.

Fig. 5 compares the upper bound solutions and numerical results of uniaxial bearing capacity factors for deeply embedded chain links with a fully bonded interface. Using an analogy of the chain link being represented as an equivalent embedded rectangular plate anchor, the normal resistance to chain link displacement, N_{max}, can be estimated by Eq. (3). By taking $L_f = W$ = 0.36 m and $d_f = d$ = 0.1 m – or in other words, by simplifying the link to being a two-dimensional plate in the *u*-*w* plane (refer

202 to Fig. 1) while assuming the link length, L, is infinitely long – $V_{max}/L_f s_u$ is calculated as 12.73.
203 Alternatively, $V_{max}/L_f s_u$ is evaluated as 12.22 by taking $L_f = L$ = 0.6 m and $d_f = d$ = 0.1 m (a two-
204 dimensional plate in the v-w plane). Merifield et al. (2003) reported a lower bound value of $V_{max}/L_f s_u$
205 = 11.9 for a deeply embedded square anchor ($z/L_f \approx 7$) with a rough interface. Three-dimensional
206 finite element analyses of plate anchors with an aspect ratio, defined as the ratio of the anchor length
207 to anchor width, of 2 and a fully bonded interface gave $V_{max}/L_f s_u$ = 13.1 for a plate thickness of zero
208 (Yang et al. 2010) and $V_{max}/L_f s_u$ = 13.29 for a plate thickness of 1/20 of the width (Wang et al. 2010a).
209 Accordingly, the normal bearing capacity factor, $N_{max}/A_w s_u$ = 12.64 determined here is within the
210 range of published results for deeply embedded rectangular plate anchors with an aspect ratio of
211 between 1 and 2. The corresponding soil flow mechanism is shown in Fig. 6(a) as both displacement
212 vectors and displacement contour plots in the u-w plane, and is evidently similar to the upper bound
213 mechanism for the deeply embedded rectangular plate anchor (see Fig. 4(a)). As the 'openings' in the
214 chain link are relatively small, there is limited capacity for soil to flow through the chain, such that
215 the mechanism is expected to be similar to that of an equivalent rectangular plate.

216 The lateral soil resistance of a displaced chain link, S_{max}, can be estimated by the upper bound solution
217 (Eq. (3)) by selecting $L_f = L$ = 0.6 m and $d_f = A_w/L$ = 0.23 m (i.e. a two-dimensional plate in the u-v
218 plane with a length of L and an equivalent thickness of A_w/L). This results in $V_{max}/L_f s_u$ = 13.21, 18.5%
219 lower than $S_{max}/A_u s_u$ = 16.21 obtained from the finite element analysis reported here. Note that A_u is
220 the normal bearing area because the u axis is treated as the normal direction when the chain link is
221 simplified as an equivalent two-dimensional plate in the u-v plane. A more appropriate interpretation
222 is to assume $L_f = W$ = 0.36 m and $d_f = d$ = 0.1 m (a two-dimensional plate in the u-w plane) in Eq. (4).
223 This gives $H_{max}/L_f s_u$ = 7.03, only 4% higher than the finite element result, $S_{max}/A_w s_u$ = 6.76, where A_w

is the corresponding normal bearing area of the equivalent two-dimensional plate in the *u*-*v* plane. The soil flow mechanism due to pure lateral displacement, *u*, is shown in Fig. 6(b), which is broadly consistent with the mechanism for a deeply embedded rectangular plate anchor under lateral displacement, as shown in Fig. 4(b).

The axial soil resistance of a displaced chain link, T_{max}, can be estimated by Eq. (4) with $L_f = L = 0.6$ m and $d_f = d = 0.1$ m (i.e. a two-dimensional plate in the *v*-*w* plane), which gives $H_{max}/L_f s_u = 5.5$, greater than $T_{max}/A_w s_u = 2.98$ obtained numerically. This difference is because the upper bound solution in O'Neill et al. (2003) is for an 'isolated' anchor, whereas the chain comprises many connected links that are 'shaded' by adjacent links in the axial direction. This can be seen in the corresponding soil flow mechanism shown in Fig. 6(c). The shading effect from the adjacent links can be demonstrated by modelling an 'isolated' chain link (i.e. without adjacent links), which resulted in $T_{max}/A_w s_u = 6.22$. Compared with $T_{max}/A_w s_u = 2.98$ for a linked chain, this 'isolated' axial bearing capacity factor is much closer to the upper bound solution, $H_{max}/L_f s_u = 5.5$, with the difference essentially due to the shading from adjacent links. The normal resistance may alternatively be evaluated as $V_{max}/L_f s_u = 16.17$ by taking $L_f = W = 0.36$ m and $d_f = A_w/W = 0.39$ m (a two dimensional plate in the *u*-*v* plane), which is greater than the finite element result, $T_{max}/A_w s_u = 12.18$ obtained in this study. This disparity is again considered to be due to the shading effect from the adjacent links.

3.2 Studless link chain

The stabilised uniaxial normal, lateral and axial soil resistances for a deeply buried studless link with a fully-bonded chain-soil interface ($z/W = 11$, $\beta = 0°$ and $\alpha = \infty$) are $N_{max} = 75.6$ kN, $S_{max} = 45.9$ kN and $T_{max} = 19.6$ kN, respectively. The projected areas A_w, A_u and A_v for the studless link chain are

0.125 m^2, 0.058 m^2 and 0.031 m^2, respectively. Dimensionless bearing capacity factors for the studless link chain can therefore be calculated as $N_{max}/A_w s_u = 12.09$, $S_{max}/A_w s_u = 7.35$ (or $S_{max}/A_u s_u = 15.83$) and $T_{max}/A_w s_u = 3.13$ (or $T_{max}/A_v s_u = 12.65$).

The normal bearing capacity factor, $N_{max}/A_w s_u = 12.09$ is 4.4% lower than that for the stud link chain, $N_{max}/A_w s_u = 12.64$. As shown above, the upper bound solution of the normal bearing capacity factor for the studless link chain is $V_{max}/L_f s_u = 12.82$, obtained by taking $L_f = W = 0.335$ m and $d_f = d = 0.1$ m; while $V_{max}/L_f s_u = 12.22$ results from taking $L_f = L = 0.6$ m and $d_f = d = 0.1$ m. The reason for the lower normal bearing capacity factor of the studless link chain relative to the stud link chain is because the absence of the stud eases soil flow through the chain link, as can be seen from the soil flow mechanism in Fig. 7(a).

Although the lateral soil resistance, S_{max}, for the stud link and studless cases is comparable, the lateral soil resistance, $S_{max}/A_w s_u = 7.35$ is 8.6% higher for the studless chain as the projected area in the normal direction, A_w, for the studless link is lower. Referring to Fig. 5, the lateral resistance can be evaluated using the upper bound solution by taking $L_f = W = 0.335$ m and $d_f = d = 0.1$ m in Eq. (4), which gives $H_{max}/L_f s_u = 7.30$, close to the numerical result of $S_{max}/A_w s_u = 7.35$. Alternatively, $V_{max}/L_f s_u = 13.06$ is determined by taking $L_f = L = 0.6$ m and $d_f = A_w/L = 0.21$ m, which is 17.5% smaller than $S_{max}/A_u s_u = 15.83$ in this paper. The lateral flow mechanism of the soil around the studless link is similar to that of the stud link chain, as shown in Fig. 6(c) and Fig. 7(c).

The finite element result for axial soil resistance is $T_{max}/A_w s_u = 3.13$. Referring to Fig. 5, the axial resistance can be evaluated using the upper bound solution by taking $L_f = L = 0.6$ m and $d_f = d = 0.1$ m (a two-dimensional plate in the *v*-*w* plane) in Eq. (4), which gives $H_{max}/L_f s_u = 5.5$. This is much higher

than the finite element result of $T_{max}/A_w s_u = 3.13$. Again, the reason for the difference is considered to be due to 'shading' from adjacent links. Alternatively, taking $L_f = W = 0.335$ m and $d_f = A_w/W = 0.37$ m leads to $V_{max}/L_f s_u = 16.26$, larger than the finite element result of $T_{max}/A_v s_u = 12.65$.

Throughout the remainder of the paper, the uniaxial bearing capacity factors are defined in terms of the projected area, A_w, i.e. $N_{n,max} = N_{max}/A_w s_u$, $N_{s,max} = S_{max}/A_w s_u$ and $N_{t,max} = T_{max}/A_w s_u$.

3.3 Effects of embedment depth, z, and link direction angle, β

Fig. 8 shows how the uniaxial bearing capacity factors vary with z/W and β for a stud link chain with a fully bonded interface (full details of other cases can be found in Table 1). The normal, lateral and axial bearing capacity factors, $N_{n,max}$, $N_{s,max}$ and $N_{t,max}$ increase with embedment depth until $z/W \geq 2.5$, but at greater depths the uniaxial bearing capacity factors reach stabilised values. Thus, the depth range of $z/W \geq 2.5$ can be considered to be 'deeply embedded'. For cases where $z/W < 2.5$, the normal bearing capacity factor $N_{n,max}$ decreases with β, while the lateral bearing capacity factor $N_{s,max}$ increases with β. This is because as β increases, the normal displacement, w, tends to mobilise less soil volume, while the lateral displacement, u, mobilises more. It is noted that β only has a very limited influence on $N_{t,max}$ as the soil area mobilised by the axial resistance, T, is concentrated around the chain links, as shown in Fig. 6(c) and Fig. 7(c). Accordingly, for the chain link on the seabed surface ($z/W = 0$), as shown in Fig. 8, the direction angle, β, has a dramatic influence on N and S but a relatively small influence on T.

3.4 Effect of interface roughness, α

To investigate the effect of interface roughness, α, on the uniaxial bearing capacity factors of chain

links, analysis cases with α = 0, 0.2, 0.4, 0.6, 0.8 and 1 were conducted. Chain link direction angles of β = 0° and 90° were considered, as shown in Table 1. Fig. 9 shows the effect of interface roughness on the normal, lateral and axial bearing capacity factors, $N_{n,\max}$, $N_{s,\max}$ and $N_{t,\max}$ for stud link chains (as an example). Fig. 9 indicates that all uniaxial bearing capacity factors $N_{n,\max}$, $N_{s,\max}$, and $N_{t,\max}$ increase with α.

Figs. 10(a) and (b) show the vector plot of the normal force (represented by normal contact force on nodes) and friction (represented by shear contact force on nodes) acting on the stud link chain under pure normal displacement, w, for α = 0 and 1. For α = 0, there are only normal forces acting on the chain as the α = 0 condition prevents friction, whereas for α = 1, both normal forces and friction act on the chain bar and stud. The normal bearing capacity factor, $N_{n,\max}$, increases by 36% from α = 0 to 1 for deep embedded cases, due to the contribution of friction.

The lateral resistance, $N_{s,\max}$, increases by 20% from α = 0 to 1 for deep embedded cases. Figs. 10(c) and (d) show the vector plot of the nodal normal force and friction under pure lateral displacement. Cross-referencing to Fig. 6(b), a large portion of the lateral resistance is from the normal force, and thus, the interface roughness, α, has a minor influence on the lateral resistance relative to normal and axial resistance.

The axial resistance, $N_{t,\max}$, is significantly affected by the interface roughness. For deep embedded cases, $N_{t,\max}$ increases by 57% from α = 0 to 1. Figs. 10(e) and (f) show the nodal normal force and friction under pure axial displacement, v. For the case using α = 0, there is no friction along the link surface and thus the normal force contributes 100% of the axial resistance, $N_{t,\max}$. For the case using α = 1, the normal force and friction both contribute to the axial resistance. Referring to Table 1, the

307 normal force accounts for 64% of the total axial resistance for deeply embedded cases, while friction
308 accounts for the remaining 36%. It is noted that existing studies (Vivatrat et al. 1982, Degenkamp and
309 Dutta 1989) proposed that the tangential soil resistance to the chain is solely equal to the friction
310 acting the chain surface. Since the normal force provides the majority of the tangential resistance, it
311 is argued here that it would be more appropriate to use a bearing capacity factor to account for the
312 tangential resistance, as discussed in detail later in the paper.

313 **4 Equivalent bearing capacity factors**

314 Two-dimensional analytical solutions for an embedded anchor line (such as Neubecker and Randolph
315 1995 and Aubeny and Chi 2014) use an equivalent bar to calculate the configuration, which requires
316 the estimation of normal, q, and tangential soil resistance, f, as shown in Eqs. (1)~(2). This section
317 discusses how to convert this study's detailed finite element results of soil resistance (i.e. N_{max}, S_{max}
318 and T_{max}) into equivalent values of q and f (normal and tangential resistance per unit length).

319 Considering that the chain link orientation alternates with adjacent links and that there is an overlap
320 length, the length of a chain link and two adjacent half links (a pair of links) is $2L - 4d = 8d$, as shown
321 in Fig. 11. The total normal force to this group of chain links can be considered as the sum of a normal
322 force and a lateral force, as shown in Eq. (5). By assuming a cylindrical bar with an equivalent
323 diameter of $E_n d$ and a length of $8d$, the total normal force is $N_q s_u E_n d \cdot 8d$, which can be written as:

324 $$q \cdot 8d = N_q s_u E_n d \cdot 8d = \left[N_{n,\max}\left(z/W, \alpha, \beta = 0°\right) + N_{s,\max}\left(z/W, \alpha, \beta = 90°\right) \right] A_w s_u \quad (5)$$

325 As noted earlier in the paper, the bar diameter multiplier, E_n, is a characteristic of the chain geometry
326 that can be calculated by equating the projected area of adjacent chain links with the normal bearing

area of a cylinder, as shown in Fig. 11(a):

$$A_w + A_u - A_{overlap} = E_n d \cdot 8d \tag{6}$$

where A_w and A_u are the projected areas of a chain link along the w and u axes, respectively (as defined earlier), and $A_{overlap}$ is the overlap area of the normal projection of the adjacent chain links. For the stud and studless links used in this study, $A_{overlap} = 2d^2$. Thus, E_n is calculated as 2.21 and 2.04 for stud and studless links, respectively. Although this is close to $E_n = 2.5$ recommended by Degenkamp and Dutta (1989), which is commonly used in the literature and design guidelines (Neubecker and Randolph 1995, Wang et al. 2010b, ABS 2017, DNV GL 2017), the lower value determined here is considered to be more appropriate for an analysis that considers the effect of adjacent chain links.

The normal bearing capacity factor N_q is then obtained by rearranging Eq. (5)

$$N_q = \frac{\left[N_{n,\max}\left(z/W, \alpha, \beta = 0°\right) + N_{s,\max}\left(z/W, \alpha, \beta = 90°\right)\right] A_w}{8E_n d^2} \tag{7}$$

The calculated values of N_q depend on embedment depth, interface roughness and chain link type, as detailed in Table 1. Figs. 12(a) and (b) show the normal bearing capacity factor, N_q, of the stud and studless link, respectively, and compare the bearing capacity factors, N_c, of the strip, square and rectangular anchors. The normal bearing capacity factor, N_q, of a chain link increases with embedment depth and reaches a stabilised value when $z/W \geq 2$, while the recommended solutions by Skempton (1951) for rectangular footings and the finite element solutions for rough strip anchor of Song et al. (2008) show N_c reaches a stabilised value when $z/B \geq 2.5$ (where B is the width).

For the chain link at the mudline ($z/W = 0$), the normal bearing capacity factor, N_q is 5.35 and 5.33

346 for $\alpha = 0$ (smooth interface) for the stud link and studless link, respectively. These results are close to
347 Skempton's (1951) solutions for rectangular footings, which are 5.28 and 5.26 when the aspect ratio
348 $L/B = 8/E_n$, where $E_n = 2.21$ and 2.04, respectively. When $z/W = 0$ and $\alpha = \infty$ (rough interface), $N_q =$
349 7.21 and 7.09, with increases of 35% and 33% relative to $\alpha = 0$ for stud links and studless links,
350 respectively. This indicates that the friction on the chain link forms a significant proportion of the
351 total resistance.

352 The range of stabilised N_q is 11.06 to 15.25 (from $\alpha = 0$ to ∞) and 11.07 to 14.88 for the stud link and
353 studless link, respectively. Stabilised values of N_c for rough strip anchors (11.62 from Song et al.
354 2008), rough square anchors (11.85 from Merifield et al.'s (2003) lower bound solutions) and rough
355 rectangular anchors with $L/B = 4$ (10.27 from Merifield et al. 2003) form a range, $N_c = 10.27$ to 11.85.
356 This range of N_c for anchors encompasses the very narrow range, $N_c = 11.06$ to 11.07 for smooth
357 chain links. In contrast, the equivalent range for rough chain links, $N_c = 14.88$ to 15.25 is beyond that
358 for the anchors due to the mobilised friction on the chain surface, as shown in Figs. 10(b) and (d).

359 Yen and Tofani (1984) carried out physical tests using chains with either 2, 4 or 6 stud links that were
360 tack-welded together and deeply embedded in clay. As shown in Fig. 12(a), the range of N_q derived
361 from Yen and Tofani's (1984) test data was 7.1 to 12.1. The upper bound value of $N_q = 12.1$ is within
362 the range, $N_q = 11.06$ to 15.25 for deeply embedded stud links in this study. As noted in Yen and
363 Tofani (1984), lower values of N_q were derived from tests in clays of lower strength, due to physical
364 length limitations of the testing equipment. Tests in higher strength clays ($s_u = 5.36$ to 7.47 kPa)
365 resulted in $N_q = 11.3$ to 11.6, which is more consistently within the range, $N_q = 11.06$ to 15.25 in this
366 study.

The total tangential force on a chain link and two adjacent half links (i.e. a pair of links) can be considered as the sum of the axial forces acting on this group of chain links, i.e. $[N_{t,\max}(z/W, \alpha, \beta = 0°) + N_{t,\max}(z/W, \alpha, \beta = 90°)]A_w s_u$. As demonstrated in the previous section, the normal force accounts for the majority of the total tangential resistance, and it is argued that it is more reasonable to treat the tangential resistance as a bearing resistance rather than pure frictional resistance. By assuming a cylindrical bar with an equivalent diameter of $E_a d$ and a length of $8d$, the axial bearing area is $\pi(E_a d)^2/4$. Thus, the resistance acting on the cross-section of the equivalent cylindrical bar is $N_a s_u \cdot \pi(E_a d)^2/4$, where N_a is the tangential bearing capacity factor of the chain link. Therefore, the total tangential force on the chain link and two adjacent half links can be written as:

$$f \cdot 8d = \pi N_a s_u \left(E_a d\right)^2 / 4 = \left[N_{t,\max}\left(z/W, \alpha, \beta = 0°\right) + N_{t,\max}\left(z/W, \alpha, \beta = 90°\right)\right] A_w s_u \tag{8}$$

E_a can be derived by treating the tangential projection area of the group of adjacent chain links as equal to the cross-sectional area of the cylindrical bar, as shown in Fig. 11(b)

$$2A_v - A_{overlap,v} = \frac{\pi\left(E_a d\right)^2}{4} \tag{9}$$

where A_v is the projected area of a chain link along the v axis and $A_{overlap,v}$ is the overlap area of the tangential projection of the adjacent chain links. For stud and studless links in this study, $A_{overlap,v} = d^2$. Thus, E_a is calculated as 2.72 and 2.57 for stud and studless links, respectively, such that Eq. (8) can be written as

$$N_a = \frac{4\left[N_{t,\max}\left(z/W, \alpha, \beta = 0°\right) + N_{t,\max}\left(z/W, \alpha, \beta = 90°\right)\right] A_w}{\pi E_a^2 d^2} \tag{10}$$

The calculated values of N_a are listed in Table 1 and shown in Figs. 12(c) and (d) for stud and studless

links, respectively, and are compared to the bearing capacity factor, N_c, for circular footings and anchors. The tangential bearing capacity factor, N_a, of chain links shows a similar trend to N_q, which provides further support to the approach adopted here of treating the axial resistance as bearing capacity. N_a increases with embedment depth and reaches stabilised values when $z/W \geq 1$, while the recommended solutions by Skempton (1951) for a circular footing and Song et al.'s (2008) finite element solutions for a rough circular anchor show that N_c reaches stabilised values when $z/B \geq 2.5$ and 1.5, respectively. For the chain link at mudline ($z/W = 0$), the tangential bearing capacity factor, N_a is 3.32 and 3.51 at $\alpha = 0$ for the stud link and studless link, respectively, increasing to 7.21 and 7.60 at $\alpha = \infty$ – hence confirming that friction has a significant effect on N_a for shallow cases.

The range of stabilised N_a is 8.77 to 14.26 (from $\alpha = 0$ to ∞) and 8.77 to 15.08 for stud link and studless links, respectively. The stabilised N_a of the rough chain link is larger than the stabilised N_c of the rough circular anchor (13.67 from Song et al. 2008 and 12.60 from Merifield et al. 2003).

Based on the tests of Yen and Tofani (1984), the range of N_a can be derived by dividing the maximum soil sliding resistance by the product of the tangential projection area (as defined in Eq. (9)) and the soil strength, i.e. $N_a = 2T_{max}/(2A_v - A_{overlap,v})s_u$. As shown in Fig. 12(c), the range of N_a derived from Yen and Tofani's (1984) test data was 8.90 to 13.98, which is in good agreement with the range, N_a = 8.77 to 14.26 determined in this study for the deeply embedded stud link chain.

The value of f/q can be obtained by dividing Eq. (8) by Eq. (5), to give $f/q = \pi N_a E_a^2/(32 N_q E_n)$. This can be interpreted as the equivalent friction coefficient, μ, used in existing embedded chain solutions (e.g. Neubecker and Randolph 1995). As shown in Table 1, f/q is in the range 0.2 to 0.4, varying with embedment depth and interface roughness, in contrast to the Neubecker and Randolph (1995)

407 analytical solution, which employs a constant value regardless of embedment depth and interface
408 roughness. It is also worth noting that the range of friction coefficient inferred from the numerical
409 results is lower than the range, f/q = 0.4 to 0.6 recommended in ABS (2017).

410 As the normal resistance, q, and tangential resistance, f, are coupled, they cannot be mobilised to their
411 maximum values simultaneously. To reduce empiricism in the selection of μ for use in analytical
412 chain solutions, an approach that allows for coupling of soil resistance components is expected to
413 provide a more accurate estimation of the chain response. Liu et al. (2023) proposed such an approach,
414 which uses the bearing capacity factors reported in this study.

415 **5 Concluding remarks**

416 This paper reports on a three-dimensional finite element modelling study that investigates soil
417 resistance to displacement of mooring chain links, with full accounting of their intricate geometry.
418 Uniaxial bearing capacity factors, $N_{n,\max}$, $N_{s,\max}$ and $N_{t,\max}$ along the normal, lateral and axial directions
419 were defined with respect to chain link type, embedment depth, link direction angle and interface
420 condition. Soil flow mechanisms at capacity are reported and provide insight into the numerical
421 results and trends obtained. The bearing capacity factors and soil flow mechanisms depend not only
422 on the link type and interface roughness, but also the shading effect of adjacent links compared with
423 the embedded anchor.

424 This study's finite element results were converted to normal and tangential soil resistance, q and f,
425 acting on an equivalent cylindrical bar. Updates to values for E_n and E_a were derived from the
426 geometry of the chain links. Equivalent bearing capacity factors, N_q and N_a were obtained based on

427 the finite element results, which reduces the empiricism in calculating q and f. N_a is considered as a
428 tangential bearing capacity factor, rather than as pure friction, as the axial chain-soil interaction
429 mechanism indicates that nodal normal forces constitute a major proportion of the axial resistance.
430 f/q was calculated to represent the friction coefficient, μ, which ranges from 0.2 to 0.4 – and it is
431 noted that q and f cannot be fully mobilised simultaneously to their maximum values. This study
432 forms the basis for an improved analytical solution for embedded chains (see Liu et al. 2024) that
433 uses the bearing capacity factors reported here, whilst allowing for the coupling of normal, lateral and
434 axial soil resistances.

435 **Data Availability Statement**

436 Some or all data, models or code that support the findings of this study are available from the
437 corresponding author upon reasonable request.

438 **Acknowledgements**

439 This research was undertaken with support from the Australian Research Council (ARC) Discovery
440 Projects (DP180103314, DP190103315) and the ARC Industrial Transformation Research Hub for
441 Offshore Floating Facilities that is funded by the Australian Research Council, Woodside Energy,
442 Shell, Bureau Veritas and Lloyds Register (Grant No. IH140100012). The corresponding author's
443 ARC Future Fellowship (FT200100457) is acknowledged. Phil Watson leads the Shell Chair in
444 Offshore Engineering research team at The University of Western Australia, which is sponsored by
445 Shell Australia. Professor Fraser Bransby at The University of Western Australia is appreciated for
446 his discussions, suggestions, and review on this study.

References

ABS. 2017. Design and installation of drag anchors and plate anchors. American Bureau of Shipping, Houston, Texas.

Aubeny, C., and Chi, C.M. 2014. Analytical model for vertically loaded anchor performance. Journal of Geotechnical and Geoenvironmental Engineering, **140**(1): 14–24. doi:10.1061/(ASCE)GT.1943-5606.0000979.

Dassault Systèmes. 2019. SIMULIA user assistance 2019: Abaqus. Dassault Systèmes Simulia Corp., Providence, Rhode Island.

Degenkamp, G., and Dutta, A. 1989. Soil resistances to embedded anchor chain in soft clay. Journal of Geotechnical Engineering, **115**(10): 1420–1438.

DNV GL. 2017. Design and installation of plate anchors in clay. DNVGL-RP-E302. Det Norske Veritas, Høvik, Norway.

Frankenmolen, S.F., White, D.J., and O'Loughlin, C.D. 2016. Chain-soil interaction in carbonate sand. *In* Proceedings of the Annual Offshore Technology Conference. Offshore Technology Conference, Houston, Texas.

Han, C., and Liu, J. 2017. A modified method to estimate chain inverse catenary profile in clay based on chain equation and chain yield envelope. Applied Ocean Research, **68**: 142–153. doi:10.1016/j.apor.2017.08.016.

Liu, W., Tian, Y., and Cassidy, M.J. 2021. An interface to numerically model undrained soil-structure interactions. Computers and Geotechnics, **138**: 104327. doi:10.1016/j.compgeo.2021.104327.

Liu, W., Tian, Y., Cassidy, M.J., and Watson, P. 2024. A new analytical approach to model embedded anchor lines based on the yield surface of soil resistance. Géotechnique. (Submitted on 16 May 2023).

Merifield, R.S., Lyamin, A. V., Sloan, S.W., and Yu, H.S. 2003. Three-Dimensional Lower Bound Solutions for Stability of Plate Anchors in Clay. Journal of Geotechnical and Geoenvironmental Engineering, **129**(3): 243–253. doi:10.1061/(asce)1090-0241(2003)129:3(243).

Neubecker, S.R., and Randolph, M.F. 1995. Profile and frictional capacity of embedded anchor chains. Journal of Geotechnical Engineering, **121**(11): 797–803. doi:10.1061/(ASCE)0733-9410(1995)121:11(797).

O'Loughlin, C.D., White, D.J., Stanier, S.A. (2017). The use of plate anchors for mooring floating facilities – a view towards unlocking cost and risk benefits. Proceedings of the 8th International Conference on Offshore Site Investigation and Geotechnics, London, UK, 2, 978-986.

O'Neill, M.P., Bransby, M.F., and Randolph, M.F. 2003. Drag anchor fluke-soil interaction in clays. Canadian Geotechnical Journal, **40**(1): 78–94. doi:10.1139/t02-096.

Rocha, M.M., Schnaid, F., Rocha, C.C.M., and Amaral, C.S. 2016. Inverse catenary load attenuation along embedded ground chain of mooring lines. Ocean Engineering, **122**: 215–226. doi:10.1016/j.oceaneng.2016.06.027.

Skempton, A.W. 1951. The bearing capacity of clays. *In* Building Research Congress. London. pp. 180–189.

Song, Z., Hu, Y., and Randolph, M.F. 2008. Numerical simulation of vertical pullout of plate anchors embedded in clay. Journal of Geotechnical and Geoenvironmental Engineering, **134**(6): 866–875. doi:10.28927/sr.421043.

Supachawarote, C., Randolph, M., and Gourvenec, S. 2004. Inclined pull-out capacity of suction caissons. *In* Proceedings of the 14th International Offshore and Polar Engineering Conference. The International Society of Offshore and Polar Engineers, Toulon, France. pp. 500–506.

Tian, Y., Randolph, M.F., and Cassidy, M.J. 2015. Analytical solution for ultimate embedment depth and potential holding capacity of plate anchors. Geotechnique, **65**(6): 517–530. doi:10.1680/geot.14.P.228.

Vivatrat, V., Valent, P.J., and Ponterio, A.A. 1982. The influence of chain friction on anchor pile design. *In* Proceedings of the 14th Annual Offshore Technology Conference. Offshore Technology Conference, Houston, Texas. pp. 153–163.

Vryhof Anchors. 2015. Anchoring manual 2015, the guide to anchoring. Schiedam, The Netherlands.

Wang, D., Hu, Y., and Randolph, M.F. 2010a. Three-Dimensional Large Deformation Finite-Element Analysis of Plate Anchors in Uniform Clay. Journal of Geotechnical and Geoenvironmental Engineering, **136**(2): 355–365. doi:10.1061/(asce)gt.1943-5606.0000210.

Wang, L.Z., Guo, Z., and Yuan, F. 2010b. Quasi-static three-dimensional analysis of suction anchor mooring system. Ocean Engineering, **37**: 1127–1138. doi:10.1016/j.oceaneng.2010.05.002.

Yang, M., Murff, J.D., and Aubeny, C.P. 2010. Undrained Capacity of Plate Anchors under General Loading. Journal of Geotechnical and Geoenvironmental Engineering, **136**(10): 1383–1393. doi:10.1061/(asce)gt.1943-5606.0000343.

Yen, B.C., and Tofani, G.D. 1984. Soil Resistance to Stud Link Chain. *In* 16th Annual Offshore Technology Conference. Offshore Technology Conference, Houston, Texas. pp. 479–488.

Figure Captions:

Fig. 1 Size of common chain links

(a) stud link

(b) studless link

Fig. 2 Finite element model

(a) deeply embedded case

(b) close-up of chain links

Fig. 3 Uniaxial resistance to a deep embedded stud link with a fully bonded interface

Fig. 4 Upper bound mechanisms for a deep embedded rectangular plate anchor

(a) at V_{max}

(b) at H_{max}

Fig. 5 Numerical results and upper bound solutions of uniaxial bearing capacity for deeply embedded chain links with fully bonded interface

Fig. 6 Soil flow mechanism for a deep embedded stud link chain

(a) under pure normal displacement w

(b) under pure lateral displacement u

(c) under pure axial displacement v

Fig. 7 Soil flow mechanism for a deep embedded studless link chain

(a) under pure normal displacement w

(b) under pure lateral displacement u

(c) under pure axial displacement v

Fig. 8 Uniaxial bearing capacity factors of stud link chain

(a) normal bearing capacity factor

(b) lateral bearing capacity factor

522 (c) axial bearing capacity factor

523 Fig. 9 Effect of interface roughness on uniaxial bearing capacity factors for the stud link chain

524 (a) normal bearing capacity factor ($\beta = 0°$)

525 (b) normal bearing capacity factor ($\beta = 90°$)

526 (c) lateral bearing capacity factor ($\beta = 0°$)

527 (d) lateral bearing capacity factor ($\beta = 90°$)

528 (e) axial bearing capacity factor ($\beta = 0°$)

529 (f) axial bearing capacity factor ($\beta = 90°$)

530 Fig. 10 Nodal normal force and friction acting on the deep embedded stud link

531 (a) under pure normal displacement w ($\alpha = 0$)

532 (b) under pure normal displacement w ($\alpha = 1$)

533 (c) under pure lateral displacement u ($\alpha = 0$)

534 (d) under pure lateral displacement u ($\alpha = 1$)

535 (e) under pure axial displacement v ($\alpha = 0$)

536 (f) under pure axial displacement v ($\alpha = 1$)

537 Fig. 11 Normal and tangential projections of the chain link and equivalent cylindrical bar

538 (a) normal projections

539 (b) tangential projections

540 Fig. 12 Comparison of the bearing capacity factors of anchor chains, anchors and footings

541 (a) N_q of stud link chain

542 (b) N_q of the studless link chain

543 (c) N_a of the stud link chain

544 (d) N_a of the studless link chain

545

546 **Table Captions:**

547 Table 1 Uniaxial bearing capacity factors and equivalent bearing capacity factors

548

549 Table 1 Uniaxial bearing capacity factors and equivalent bearing capacity factors

Link shape	Embed-ment depth z/W	Interface roughness α	Direction angle β	Uniaxial bearing capacity factors			Normal bearing capacity factor	Tangential bearing capacity factor	$f/q = \pi N_a E_a^2/(32 N_q E_n)$
				$N_{n,\max}$	$N_{s,\max}$	$N_{t,\max}$	N_q	N_a	
Stud link	0	0	0°	4.11	1.47	0.90	5.35	3.32	0.20
			90°	0.33	2.69	0.49			
		0.2	0°	4.54	1.70	1.05	5.81	4.38	0.25
			90°	0.48	2.84	0.79			
		0.4	0°	4.88	1.89	1.19	6.16	5.41	0.29
			90°	0.62	2.95	1.07			
		0.6	0°	5.16	2.08	1.33	6.44	6.18	0.32
			90°	0.75	3.03	1.26			
		0.8	0°	5.38	2.23	1.40	6.65	6.55	0.32
			90°	0.84	3.08	1.33			
		1	0°	5.53	2.36	1.44	6.81	6.92	0.33
			90°	0.91	3.14	1.45			
		∞	0°	5.95	2.62	1.50	7.21	7.21	0.33
			90°	0.85	3.22	1.51			
			15°	4.63	2.63	1.30	-	-	-
			30°	2.38	2.72	1.42	-	-	-
			45°	1.28	2.77	1.46	-	-	-
			60°	0.96	2.85	1.53	-	-	-
			75°	0.90	3.21	1.24	-	-	-
	0.64	0	0°	8.24	2.91	1.87	9.53	8.44	0.29
			90°	6.16	3.88	1.66			
		0.2	0°	8.71	2.90	2.16	10.01	9.98	0.33
			90°	6.64	4.02	2.01			
		0.4	0°	8.92	2.91	2.35	10.26	11.04	0.35
			90°	6.96	4.14	2.26			
		0.6	0°	9.19	2.97	2.52	10.42	12.03	0.38
			90°	7.20	4.06	2.51			
		0.8	0°	9.34	3.06	2.58	10.53	12.66	0.40
			90°	7.36	4.06	2.72			
		1	0°	9.41	3.14	2.61	10.62	13.04	0.40
			90°	7.45	4.10	2.84			
		∞	0°	9.58	3.25	2.68	10.89	13.39	0.40
			90°	7.69	4.27	2.92			
			15°	9.09	3.43	2.68	-	-	-
			30°	8.67	3.44	2.68	-	-	-
			45°	8.33	3.52	2.76	-	-	-

Link shape	Embed-ment depth z/W	Interface roughness α	Direction angle β	Uniaxial bearing capacity factors			Normal bearing capacity factor	Tangential bearing capacity factor	$f/q = \pi N_a E_a^2/(32 N_q E_n)$
				$N_{n,\max}$	$N_{s,\max}$	$N_{t,\max}$	N_q	N_a	
Stud link	0.64	∞	60°	7.95	3.63	2.76	-	-	-
			75°	7.62	3.95	2.93	-	-	-
	1	0	0°	8.62	3.43	1.83	10.67	8.77	0.27
			90°	8.09	4.95	1.83			
		0.2	0°	9.38	3.38	2.14	11.38	10.25	0.30
			90°	8.49	5.10	2.14			
		0.4	0°	9.89	3.39	2.39	11.84	11.43	0.32
			90°	8.73	5.17	2.39			
		0.6	0°	10.20	3.41	2.59	12.10	12.39	0.34
			90°	8.89	5.19	2.59			
		0.8	0°	10.41	3.51	2.75	12.26	13.17	0.35
			90°	8.94	5.18	2.75			
		1	0°	10.52	3.69	2.87	12.35	13.73	0.37
			90°	9.01	5.19	2.87			
		∞	0°	10.72	3.70	2.98	12.63	14.26	0.37
			90°	9.06	5.35	2.98			
			15°	10.17	3.77	2.98	-	-	-
			30°	9.74	3.93	2.98	-	-	-
			45°	9.54	4.22	2.98	-	-	-
			60°	9.33	4.79	2.98	-	-	-
			75°	9.09	5.08	2.98	-	-	-
	1.5	0	0°	8.54	4.81	1.83	11.03	8.77	0.26
			90°	8.61	5.49	1.83			
		0.2	0°	9.44	4.82	2.14	12.03	10.25	0.28
			90°	9.37	5.86	2.14			
		0.4	0°	10.19	4.83	2.39	12.81	11.43	0.29
			90°	9.86	6.11	2.39			
		0.6	0°	10.81	4.84	2.59	13.40	12.39	0.30
			90°	10.20	6.24	2.59			
		0.8	0°	11.30	4.84	2.75	13.83	13.17	0.31
			90°	10.44	6.29	2.75			
		1	0°	11.70	4.91	2.87	14.12	13.73	0.32
			90°	10.56	6.26	2.87			
		∞	0°	12.37	4.98	2.98	14.66	14.26	0.32
			90°	10.46	6.28	2.98			
			15°	11.99	5.01	2.98	-	-	-
			30°	11.63	5.14	2.98	-	-	-

Link shape	Embed-ment depth z/W	Interface roughness α	Direction angle β	Uniaxial bearing capacity factors			Normal bearing capacity factor	Tangential bearing capacity factor	$f/q = \pi N_a E_a^2/(32 N_q E_n)$
				$N_{n,\max}$	$N_{s,\max}$	$N_{t,\max}$	N_q	N_a	
Stud link	1.5	∞	45°	11.31	5.35	2.98	-	-	-
			60°	10.86	5.62	2.98	-	-	-
			75°	10.57	5.95	2.98	-	-	-
	2	0	0°	8.54	5.50	1.83	11.03	8.77	0.26
			90°	8.54	5.50	1.83			
		0.2	0°	9.42	5.86	2.14	12.04	10.25	0.28
			90°	9.44	5.89	2.14			
		0.4	0°	10.14	5.94	2.39	12.82	11.43	0.29
			90°	10.23	6.17	2.39			
		0.6	0°	10.73	5.95	2.59	13.44	12.39	0.30
			90°	10.77	6.37	2.59			
		0.8	0°	11.24	5.94	2.75	13.93	13.17	0.31
			90°	11.17	6.49	2.75			
		1	0°	11.66	5.94	2.87	14.32	13.73	0.32
			90°	11.45	6.55	2.87			
		∞	0°	12.64	5.86	2.98	15.25	14.26	0.31
			90°	11.95	6.75	2.98			
			15°	12.66	5.91	2.98	-	-	-
			30°	12.58	6.06	2.98	-	-	-
			45°	12.41	6.33	2.98	-	-	-
			60°	12.17	6.58	2.98	-	-	-
			75°	12.00	6.74	2.98	-	-	-
	2.5	0	0°	8.55	5.50	1.83	11.05	8.77	0.26
			90°	8.54	5.50	1.83			
		0.2	0°	9.42	5.89	2.14	12.04	10.25	0.28
			90°	9.42	5.89	2.14			
		0.4	0°	10.14	6.17	2.39	12.82	11.43	0.29
			90°	10.14	6.17	2.39			
		0.6	0°	10.73	6.37	2.59	13.44	12.39	0.30
			90°	10.73	6.37	2.59			
		0.8	0°	11.23	6.49	2.75	13.93	13.17	0.31
			90°	11.24	6.49	2.75			
		1	0°	11.66	6.55	2.87	14.32	13.73	0.32
			90°	11.66	6.55	2.87			
		∞	0°	12.64	6.69	2.98	15.25	14.26	0.31
			90°	12.66	6.76	2.98			
			15°	12.64	6.72	2.98	-	-	-

Link shape	Embed-ment depth z/W	Interface roughness α	Direction angle β	Uniaxial bearing capacity factors			Normal bearing capacity factor	Tangential bearing capacity factor	$f/q = \pi N_a E_a^2/(32 N_q E_n)$
				$N_{n,\max}$	$N_{s,\max}$	$N_{t,\max}$	N_q	N_a	
Stud link	2.5	∞	30°	12.64	6.77	2.98	-	-	-
			45°	12.65	6.81	2.98	-	-	-
			60°	12.65	6.79	2.98	-	-	-
			75°	12.66	6.76	2.98	-	-	-
	≥ 3[a]	0	N/A[b]	8.57	5.50	1.83	11.06	8.77	0.26
		0.2		9.42	5.92	2.14	12.06	10.25	0.28
		0.4		10.14	6.20	2.39	12.85	11.43	0.29
		0.6		10.73	6.40	2.59	13.47	12.39	0.30
		0.8		11.24	6.53	2.75	13.97	13.17	0.31
		1		11.66	6.60	2.87	14.35	13.73	0.31
		∞		12.64	6.76	2.98	15.25	14.26	0.31
Studless link	0	0	0°	4.07	1.56	0.97	5.33	3.51	0.21
			90°	0.11	2.89	0.49			
		0.2	0°	4.48	1.82	1.18	5.74	4.70	0.26
			90°	0.26	3.01	0.77			
		0.4	0°	4.77	2.05	1.37	6.05	5.63	0.30
			90°	0.41	3.13	0.96			
		0.6	0°	5.01	2.26	1.49	6.31	6.41	0.32
			90°	0.54	3.23	1.17			
		0.8	0°	5.19	2.43	1.54	6.52	6.83	0.33
			90°	0.63	3.32	1.29			
		1	0°	5.34	2.58	1.57	6.69	7.27	0.35
			90°	0.72	3.39	1.45			
		∞	0°	5.70	2.84	1.60	7.09	7.60	0.34
			90°	0.67	3.55	1.56			
			15°	4.53	2.91	1.49	-	-	-
			30°	2.52	2.97	1.48	-	-	-
			45°	1.36	2.96	1.56	-	-	-
			60°	0.92	2.99	1.57	-	-	-
			75°	0.66	3.50	1.37	-	-	-
	0.64	0	0°	8.32	3.29	1.84	9.76	8.58	0.28
			90°	6.31	4.42	1.72			
		0.2	0°	8.91	3.27	2.20	10.28	10.32	0.32
			90°	6.82	4.51	2.09			
		0.4	0°	9.23	3.32	2.44	10.62	11.57	0.35
			90°	7.15	4.63	2.37			

Link shape	Embed-ment depth z/W	Interface roughness α	Direction angle β	Uniaxial bearing capacity factors			Normal bearing capacity factor	Tangential bearing capacity factor	$f/q = \pi N_a E_a^2/(32 N_q E_n)$
				$N_{n,\max}$	$N_{s,\max}$	$N_{t,\max}$	N_q	N_a	
Studless link	0.64	0.6	0°	9.46	3.42	2.65	10.86	12.69	0.37
			90°	7.40	4.72	2.62			
		0.8	0°	9.65	3.54	2.80	11.02	13.56	0.39
			90°	7.56	4.74	2.83			
		1	0°	9.74	3.66	2.87	11.13	14.13	0.40
			90°	7.66	4.79	3.00			
		∞	0°	9.96	3.71	2.92	11.43	14.53	0.40
			90°	7.97	4.96	3.12			
			15°	9.54	3.96	2.94	-	-	-
			30°	9.49	3.84	2.97	-	-	-
			45°	8.84	3.92	2.98	-	-	-
			60°	8.51	4.02	3.09	-	-	-
			75°	7.86	4.47	3.10	-	-	-
	1	0	0°	8.58	3.99	1.82	10.84	8.78	0.26
			90°	8.19	5.57	1.82			
		0.2	0°	9.43	3.95	2.17	11.56	10.46	0.29
			90°	8.70	5.67	2.17			
		0.4	0°	9.94	4.00	2.44	12.06	11.76	0.31
			90°	8.98	5.81	2.44			
		0.6	0°	10.29	4.09	2.67	12.42	12.88	0.33
			90°	9.20	5.93	2.67			
		0.8	0°	10.59	4.22	2.86	12.68	13.79	0.35
			90°	9.21	5.97	2.86			
		1	0°	10.78	4.36	3.01	12.87	14.49	0.36
			90°	9.28	6.02	3.01			
		∞	0°	11.13	4.18	3.13	13.25	15.08	0.36
			90°	9.55	6.18	3.13			
			15°	10.65	4.24	3.13	-	-	-
			30°	10.35	4.45	3.13	-	-	-
			45°	10.17	4.81	3.13	-	-	-
			60°	9.83	5.31	3.13	-	-	-
			75°	9.60	5.80	3.13	-	-	-
	1.5	0	0°	8.46	5.50	1.82	11.06	8.77	0.25
			90°	8.55	5.98	1.82			
		0.2	0°	9.33	5.48	2.17	11.93	10.46	0.28
			90°	9.38	6.24	2.17			

Link shape	Embed-ment depth z/W	Interface roughness α	Direction angle β	Uniaxial bearing capacity factors			Normal bearing capacity factor	Tangential bearing capacity factor	$f/q = \pi N_a E_a^2/(32 N_q E_n)$
				$N_{n,\max}$	$N_{s,\max}$	$N_{t,\max}$	N_q	N_a	
Studless link	1.5	0.4	0°	9.97	5.52	2.44	12.61	11.76	0.30
			90°	9.90	6.49	2.44			
		0.6	0°	10.47	5.57	2.67	13.15	12.88	0.31
			90°	10.23	6.70	2.67			
		0.8	0°	10.94	5.65	2.86	13.60	13.79	0.32
			90°	10.53	6.82	2.86			
		1	0°	11.31	5.79	3.01	13.98	14.49	0.33
			90°	10.71	6.94	3.01			
		∞	0°	12.14	5.77	3.13	14.82	15.08	0.32
			90°	10.92	7.21	3.13			
			15°	11.95	5.82	3.13	-	-	-
			30°	11.69	6.02	3.13	-	-	-
			45°	11.47	6.31	3.13	-	-	-
			60°	11.17	6.65	3.13	-	-	-
			75°	10.98	6.96	3.13	-	-	-
	2	0	0°	8.46	5.98	1.82	11.06	8.77	0.25
			90°	8.46	5.99	1.82			
		0.2	0°	9.33	6.25	2.17	11.93	10.46	0.28
			90°	9.33	6.25	2.17			
		0.4	0°	9.96	6.50	2.44	12.61	11.76	0.30
			90°	9.96	6.50	2.44			
		0.6	0°	10.46	6.70	2.67	13.15	12.88	0.31
			90°	10.48	6.71	2.67			
		0.8	0°	10.92	6.75	2.86	13.61	13.79	0.32
			90°	10.98	6.84	2.86			
		1	0°	11.26	6.80	3.01	13.98	14.49	0.33
			90°	11.33	7.00	3.01			
		∞	0°	12.09	6.91	3.13	14.88	15.08	0.32
			90°	11.99	7.34	3.13			
			15°	12.09	6.96	3.13	-	-	-
			30°	12.10	7.10	3.13	-	-	-
			45°	12.14	7.29	3.13	-	-	-
			60°	12.10	7.36	3.13	-	-	-
			75°	12.02	7.35	3.13	-	-	-
	2.5	0	0°	8.46	5.99	1.82	11.06	8.77	0.25
			90°	8.46	5.99	1.82			

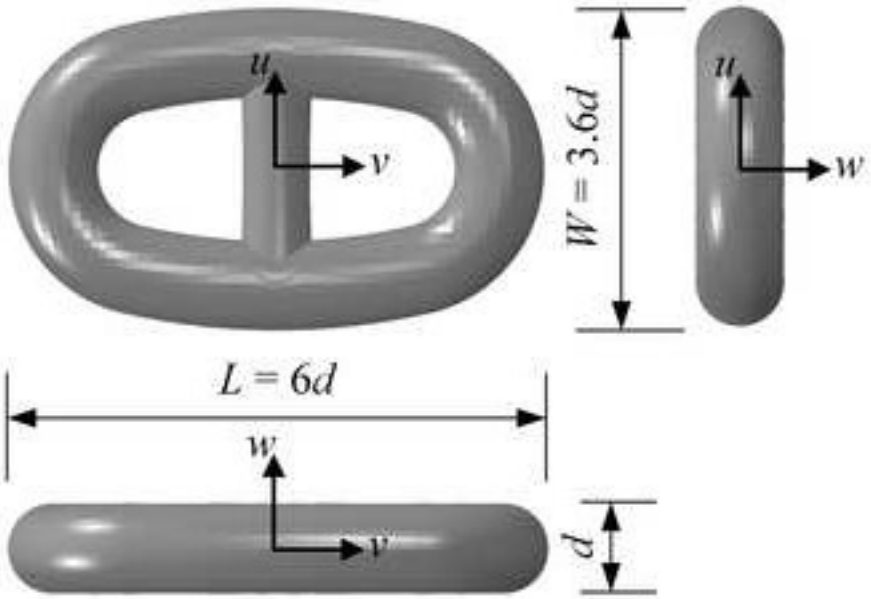
Link shape	Embed-ment depth z/W	Interface roughness α	Direction angle β	Uniaxial bearing capacity factors			Normal bearing capacity factor	Tangential bearing capacity factor	$f/q = \pi N_a E_a^2/(32 N_q E_n)$
				$N_{n,\max}$	$N_{s,\max}$	$N_{t,\max}$	N_q	N_a	
Studless link	2.5	0.2	0°	9.33	6.25	2.17	11.93	10.46	0.28
			90°	9.33	6.25	2.17			
		0.4	0°	9.96	6.50	2.44	12.61	11.76	0.30
			90°	9.96	6.50	2.44			
		0.6	0°	10.46	6.72	2.67	13.15	12.88	0.31
			90°	10.46	6.72	2.67			
		0.8	0°	10.92	6.85	2.86	13.61	13.79	0.32
			90°	10.92	6.84	2.86			
		1	0°	11.26	7.01	3.01	13.98	14.49	0.33
			90°	11.25	7.00	3.01			
		∞	0°	12.09	7.35	3.13	14.88	15.08	0.32
			90°	12.09	7.35	3.13			
			15°	12.09	7.35	3.13	-	-	-
			30°	12.09	7.36	3.13	-	-	-
			45°	12.10	7.38	3.13	-	-	-
			60°	12.09	7.36	3.13	-	-	-
			75°	12.09	7.35	3.13	-	-	-
	≥ 3[a]	0	N/A[b]	8.45	6.00	1.82	11.07	8.77	0.25
		0.2		9.32	6.27	2.17	11.94	10.46	0.28
		0.4		9.95	6.53	2.44	12.62	11.76	0.30
		0.6		10.46	6.75	2.67	13.18	12.88	0.31
		0.8		10.92	6.88	2.86	13.64	13.79	0.32
		1		11.25	7.04	3.01	14.01	14.49	0.33
		∞		12.09	7.35	3.13	14.88	15.08	0.32

550 *a* – deeply embedded scenario

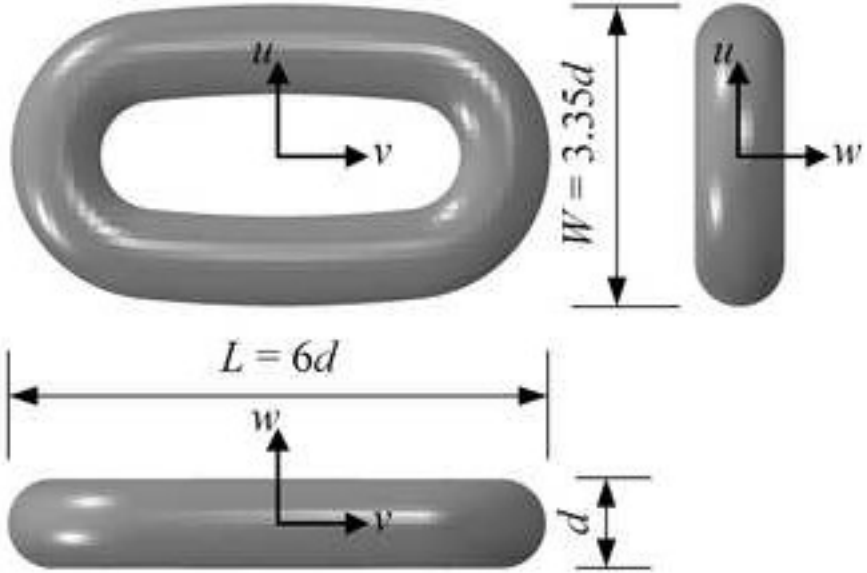
551 *b* – direction angle β has no difference for the deeply embedded scenario

552

Click here to access/download;Figure;Fig1.tif

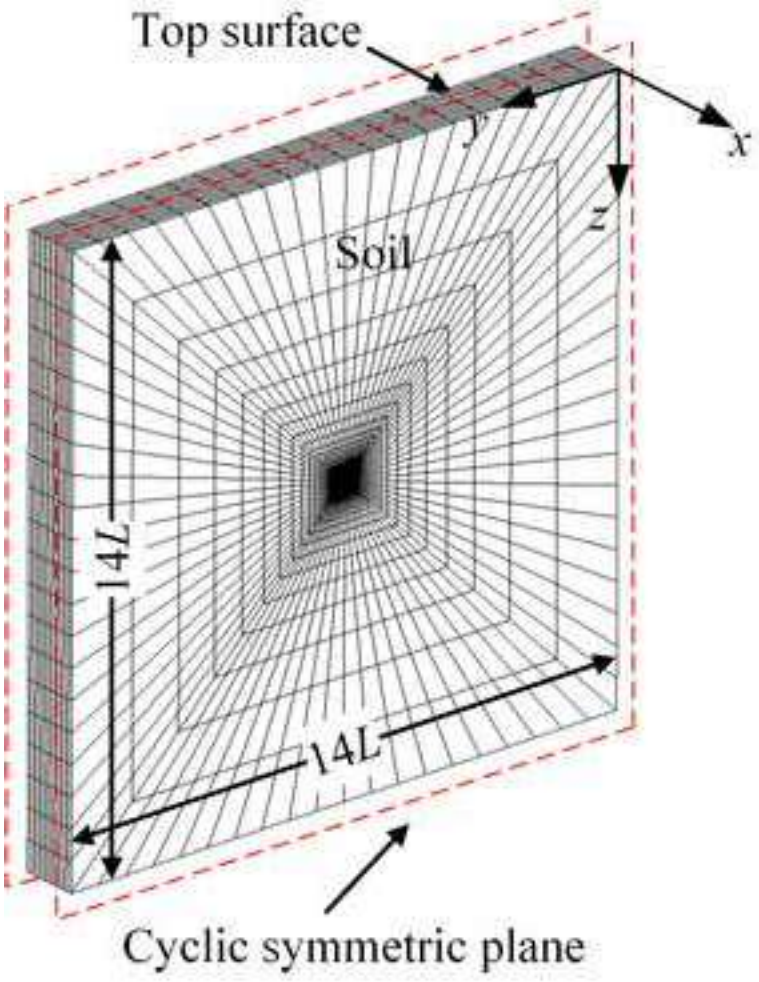


(a)

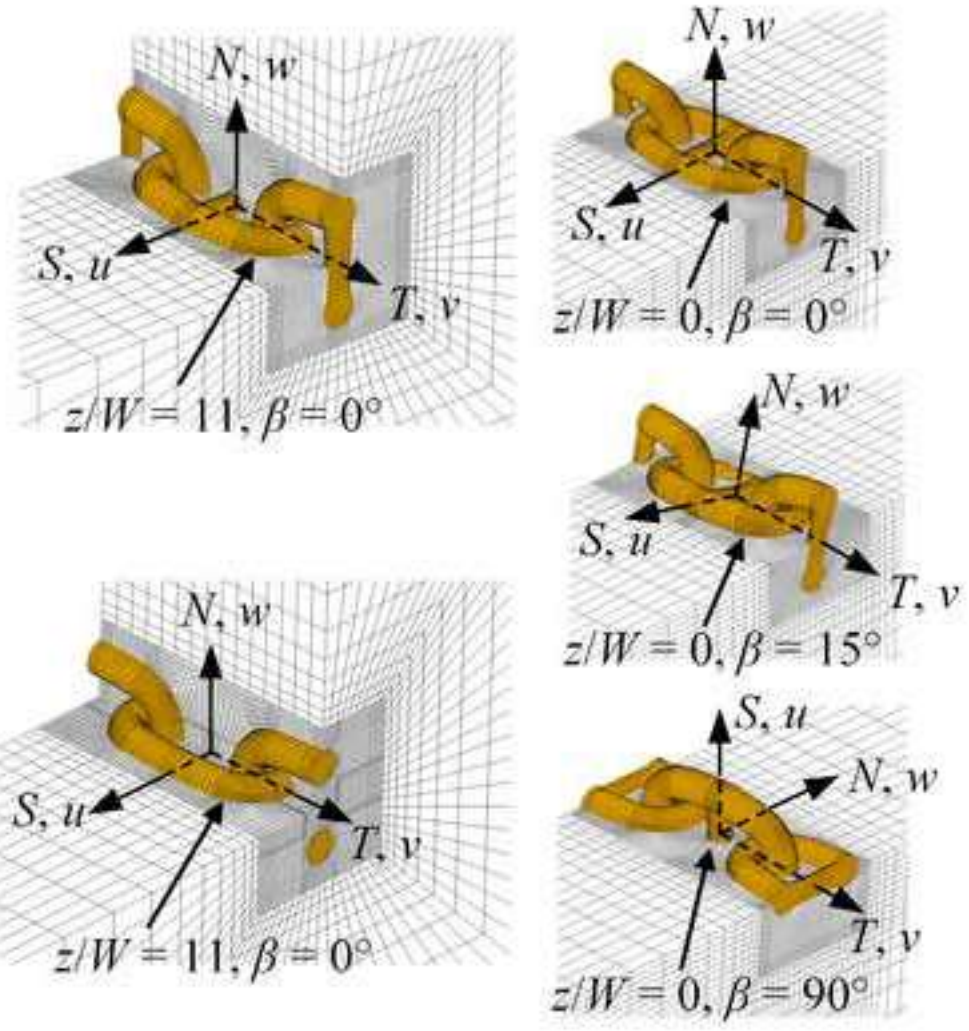


(b)

Click here to access/download;Figure;Fig2.tif



(a)



(b)

Figure3

Click here to access/download;Figure;Fig3.tif

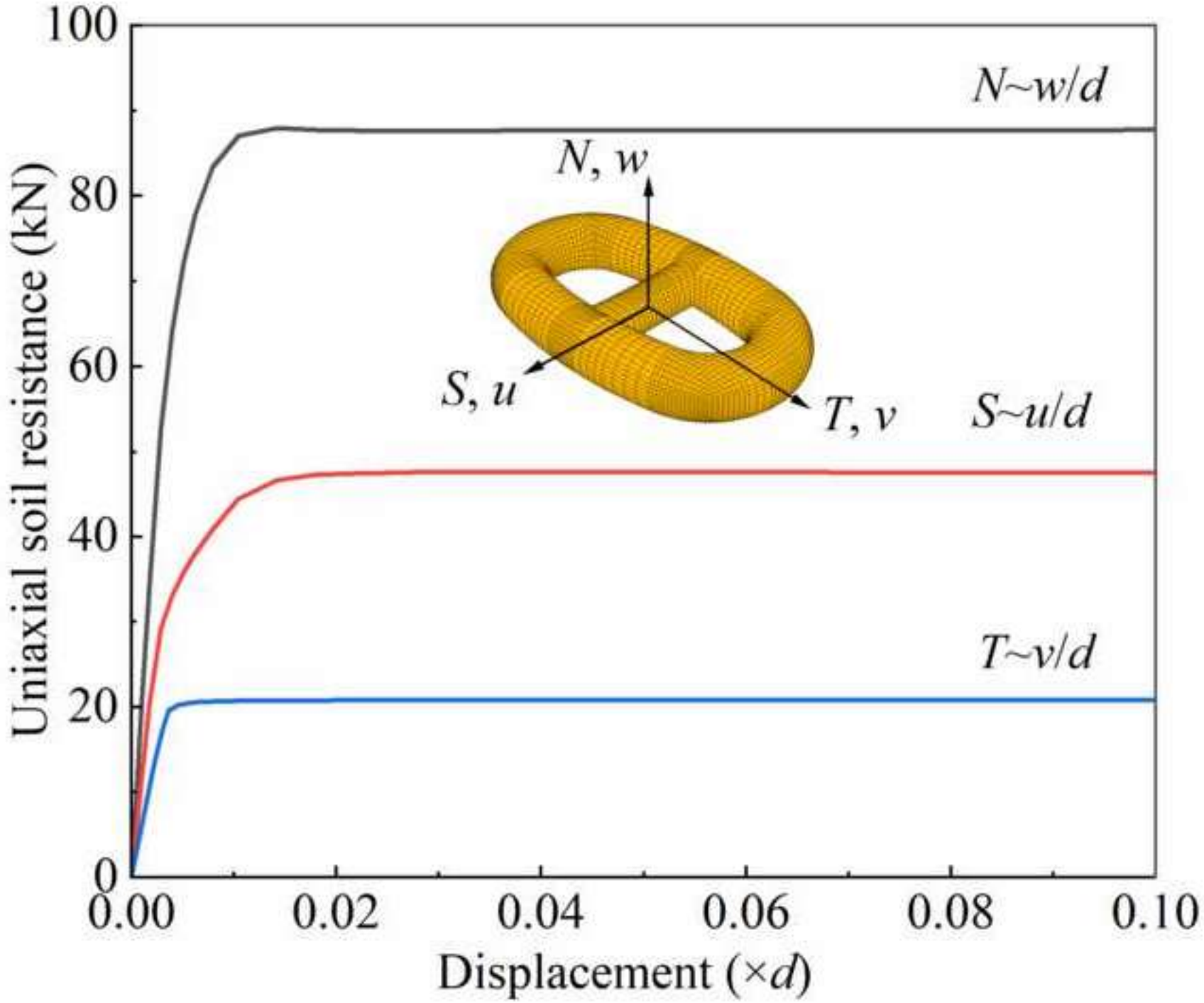
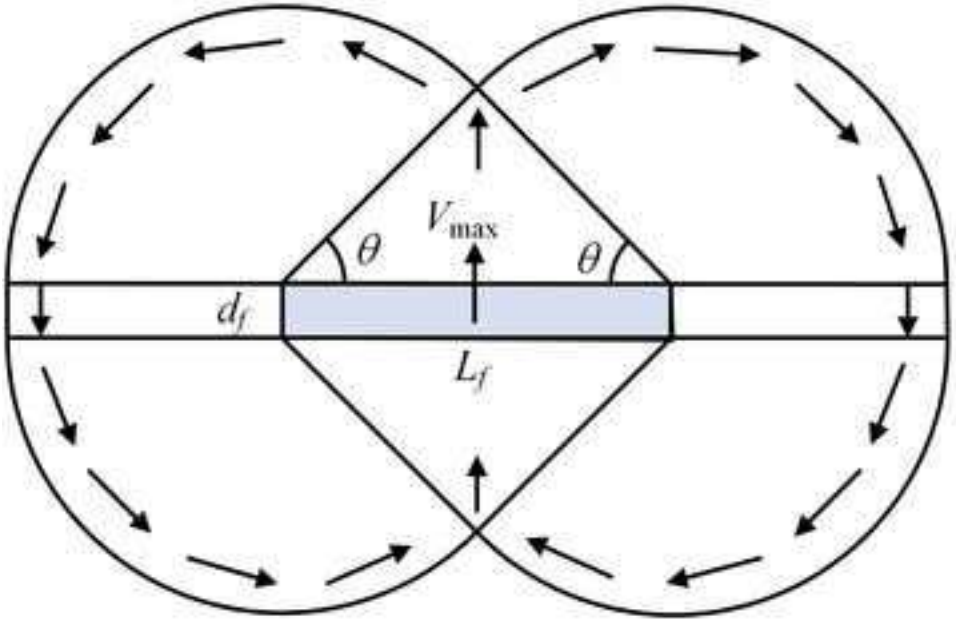
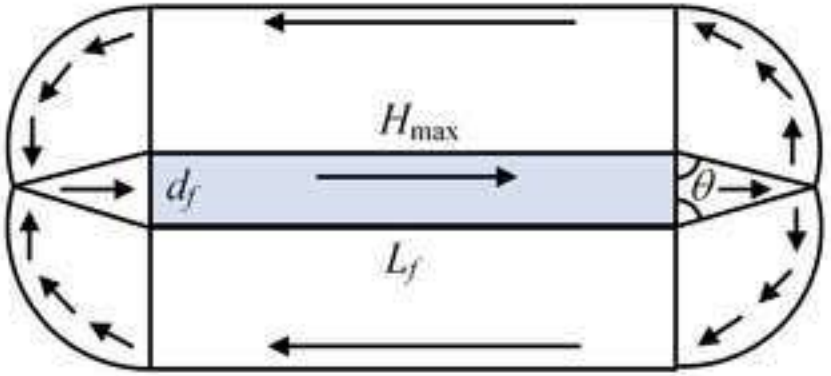


Figure4

Click here to access/download;Figure;Fig4.tif

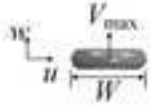
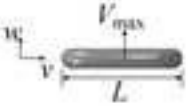
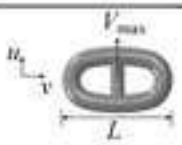
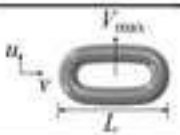
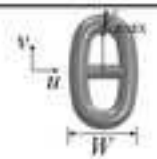


(a)

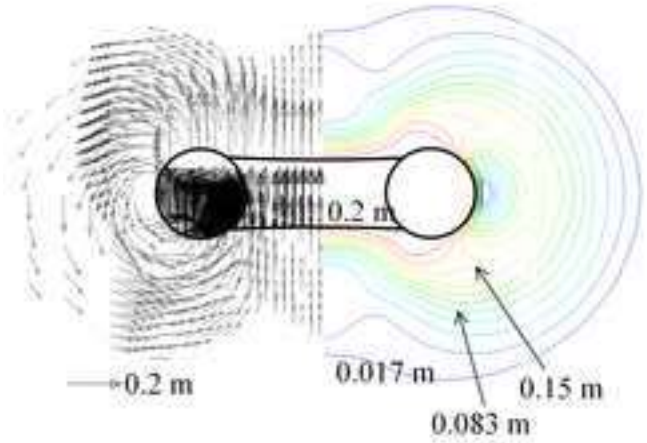


(b)

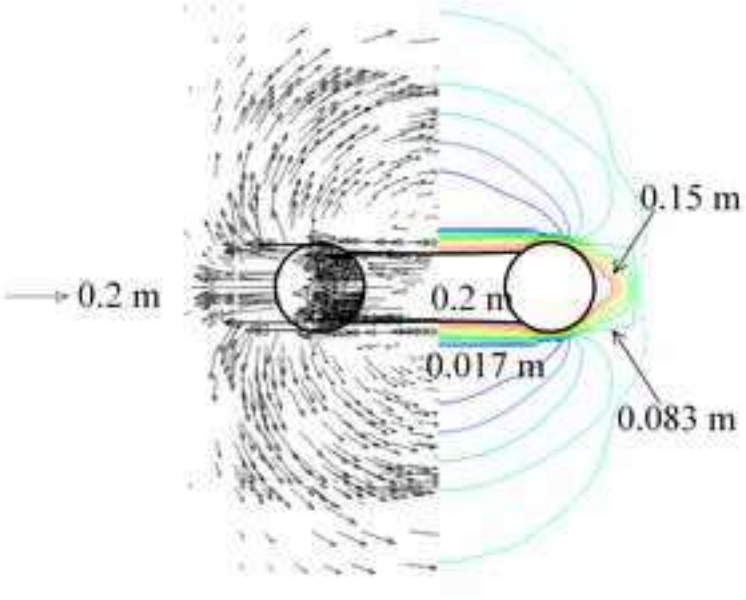
Click here to access/download;Figure;Fig5.tif

Uniaxal bearing capacity	Link type	Numerical results	O'Neill et al.'s (2003) solution				
			Calculation diagram	L_f	d_f	$V_{max}/L_f s_u$	$H_{max}/L_f s_u$
N_{max}	Stud	$N_{max}/A_w s_u = 12.64$		W	d	12.73	-
	Studless	$N_{max}/A_w s_u = 12.09$				12.82	-
	Stud	$N_{max}/A_w s_u = 12.64$		L	d	12.22	-
	Studless	$N_{max}/A_w s_u = 12.09$				12.22	-
S_{max}	Stud	$S_{max}/A_u s_u = 16.21$		L	A_w/L	13.21	-
	Studless	$S_{max}/A_u s_u = 15.83$		L	A_w/L	13.06	-
	Stud	$S_{max}/A_w s_u = 6.76$		W	d	-	7.03
	Studless	$S_{max}/A_w s_u = 7.35$				-	7.30
T_{max}	Stud	$T_{max}/A_w s_u = 2.98$		L	d	-	5.5
	Studless	$T_{max}/A_w s_u = 3.13$				-	5.5
	Stud	$T_{max}/A_v s_u = 12.18$		W	A_w/W	16.17	-
	Studless	$T_{max}/A_v s_u = 12.65$		W	A_w/W	16.26	-

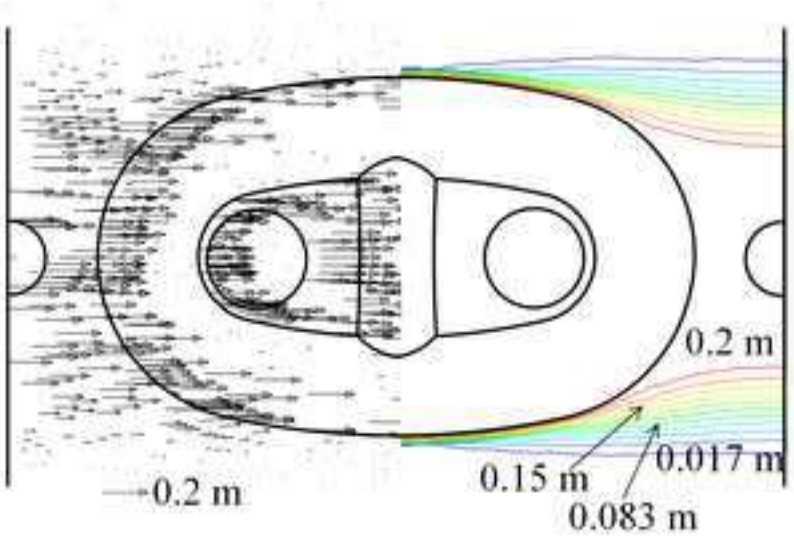
Click here to access/download;Figure;Fig6.tif



(a)



(b)



(c)

Click here to access/download;Figure;Fig7.tif

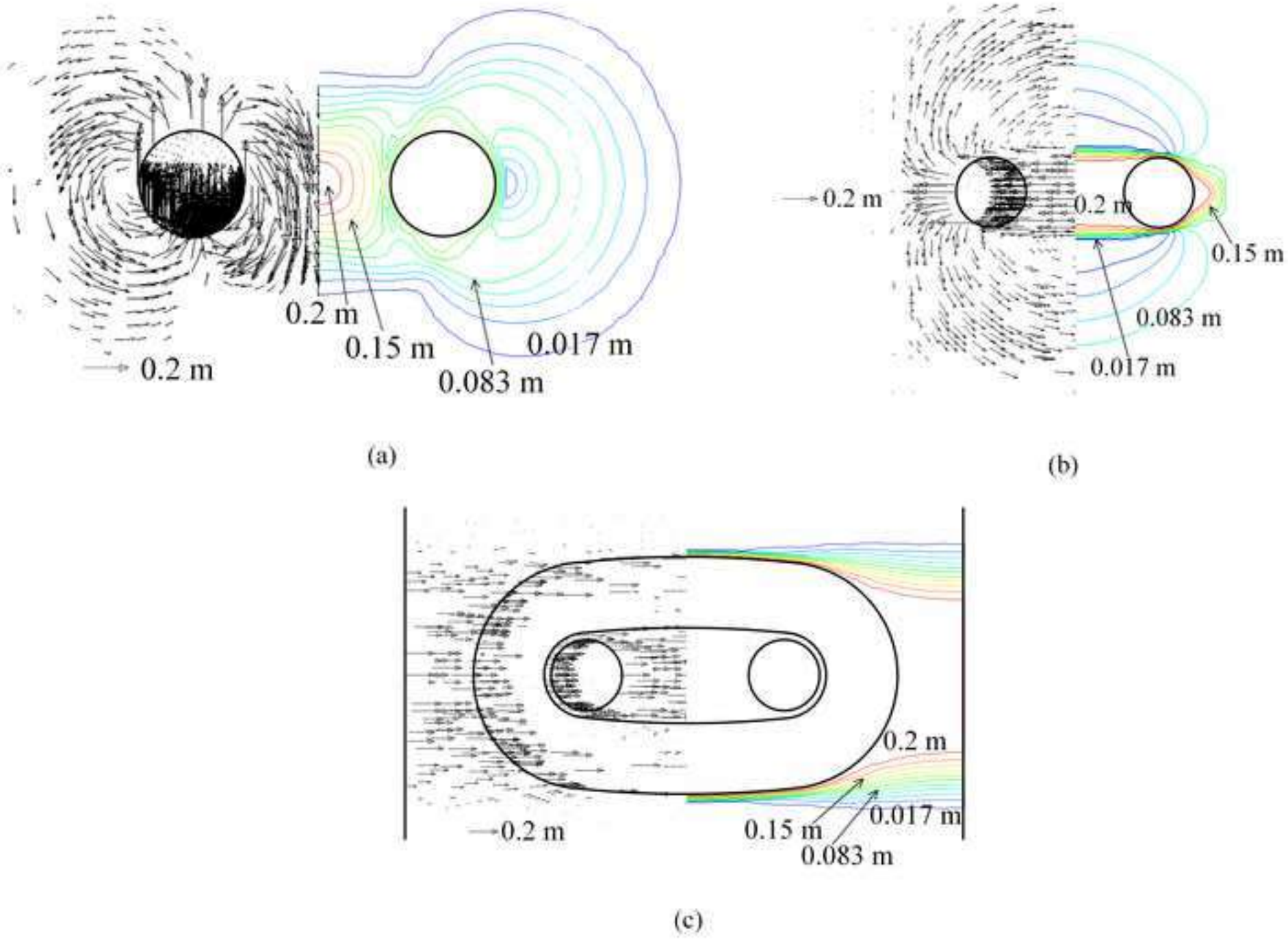


Figure8a

Click here to access/download;Figure;Fig8(a).tif

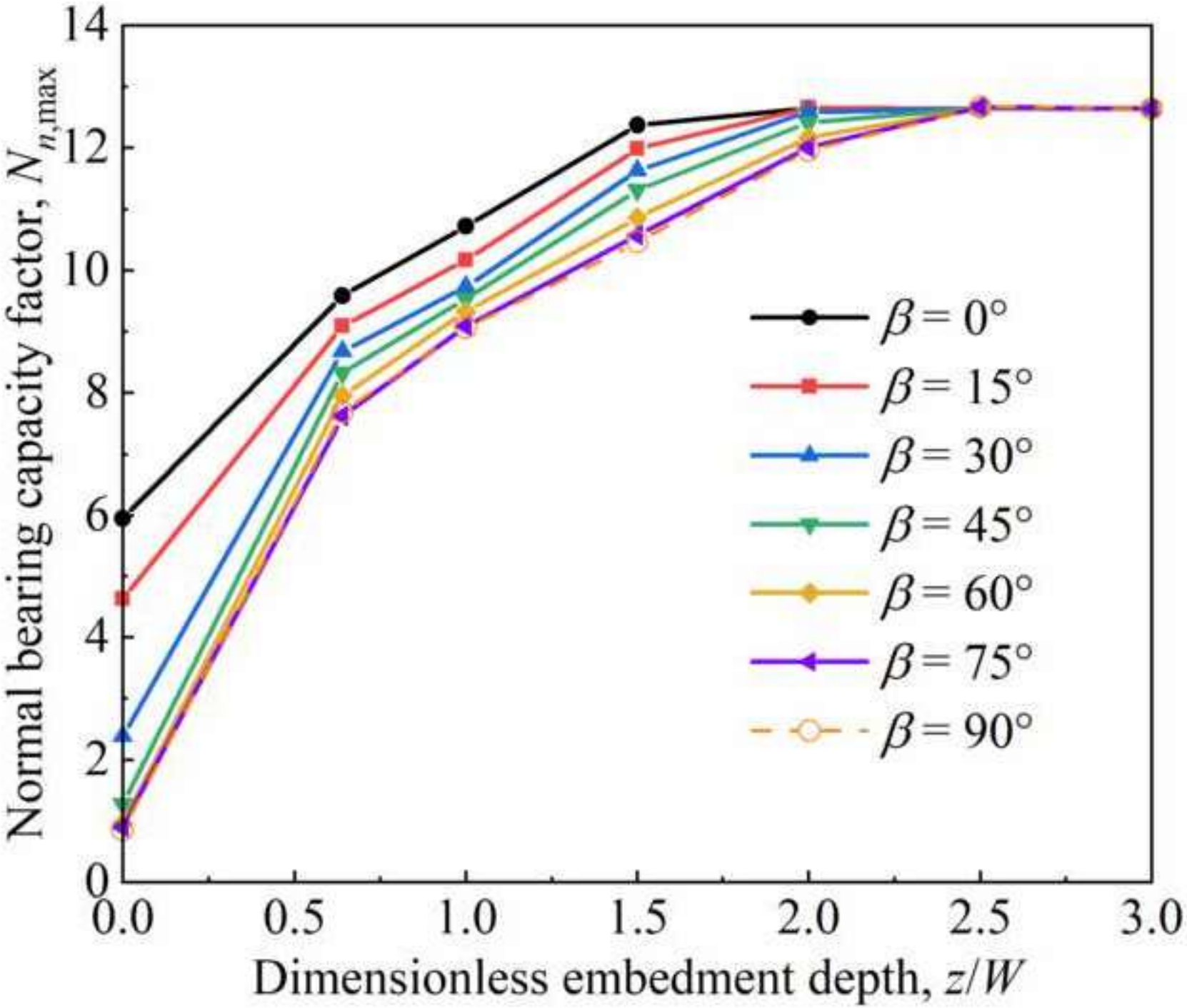


Figure8b

Click here to access/download;Figure;Fig8(b).tif

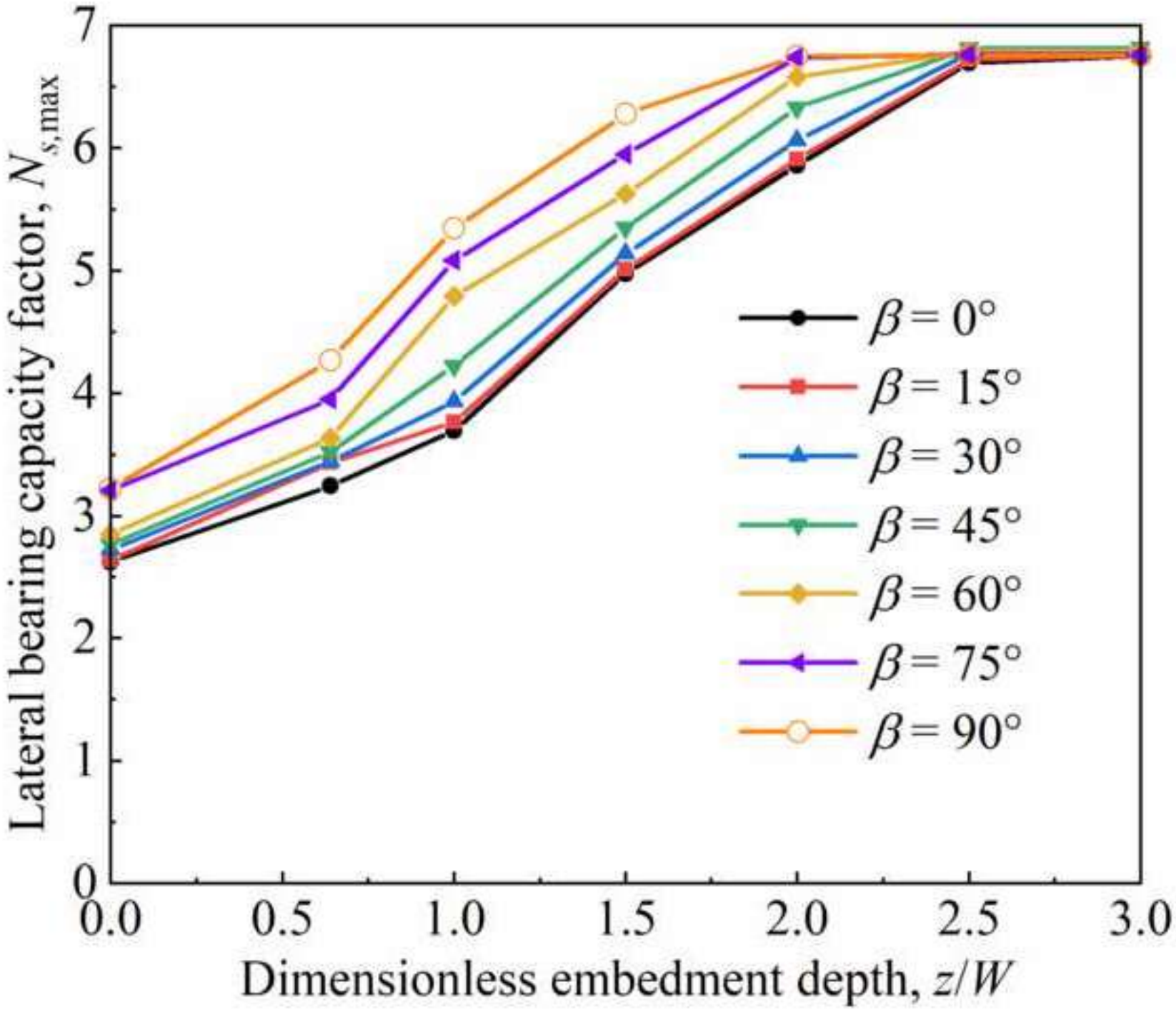


Figure8c

Click here to access/download;Figure;Fig8(c).tif

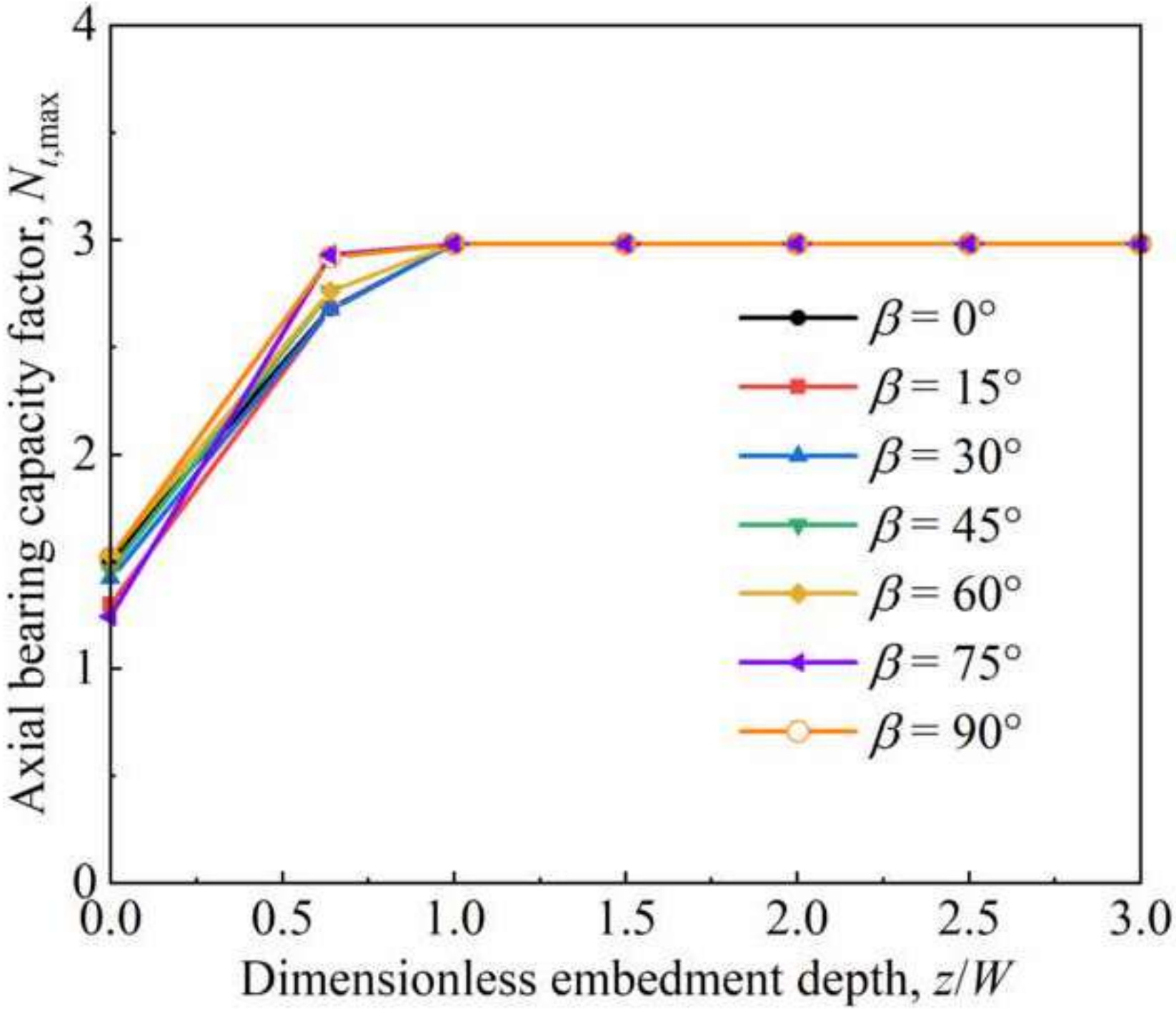


Figure9a

Click here to access/download;Figure;Fig9(a).tif

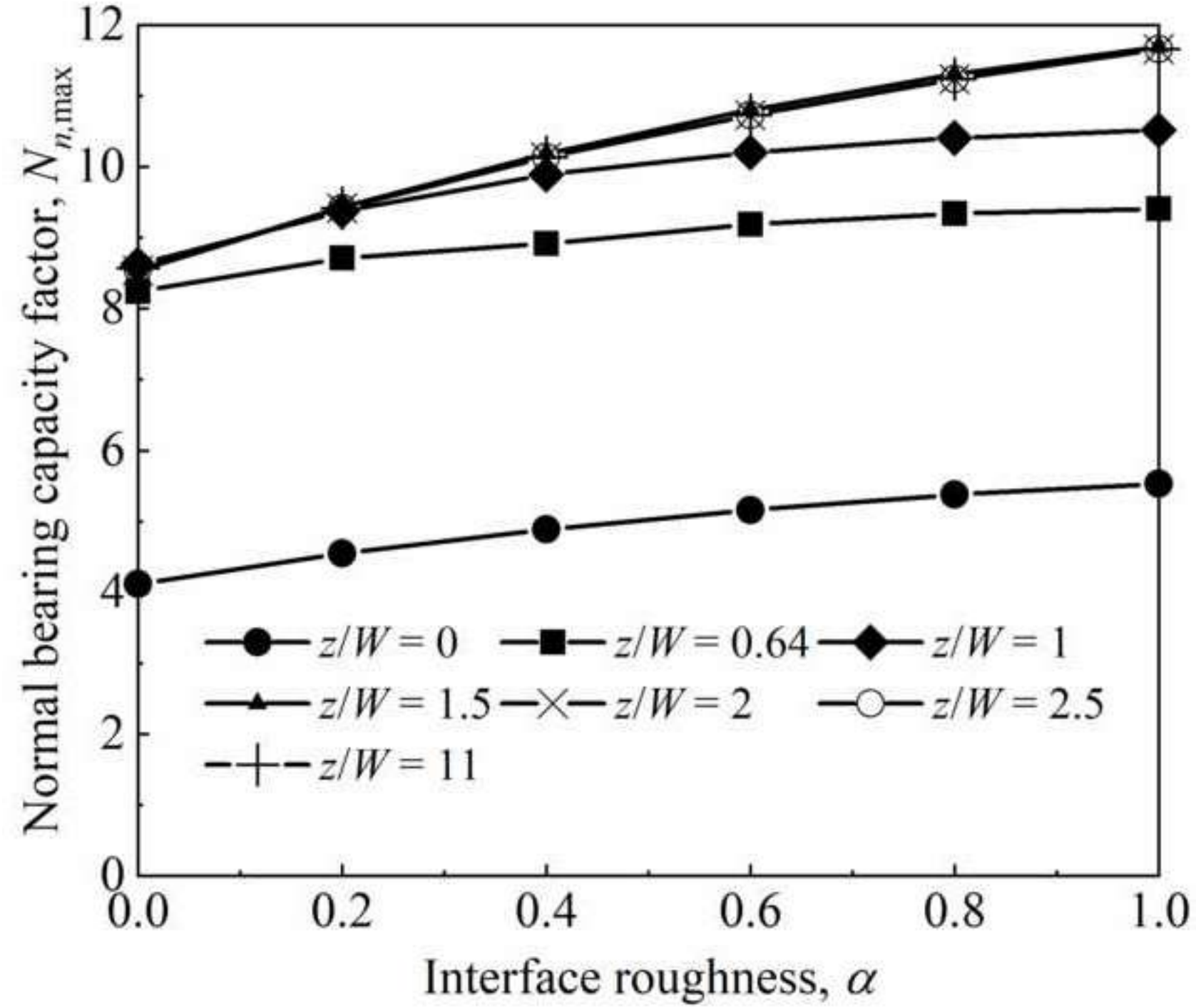


Figure9b

Click here to access/download;Figure;Fig9(b).tif

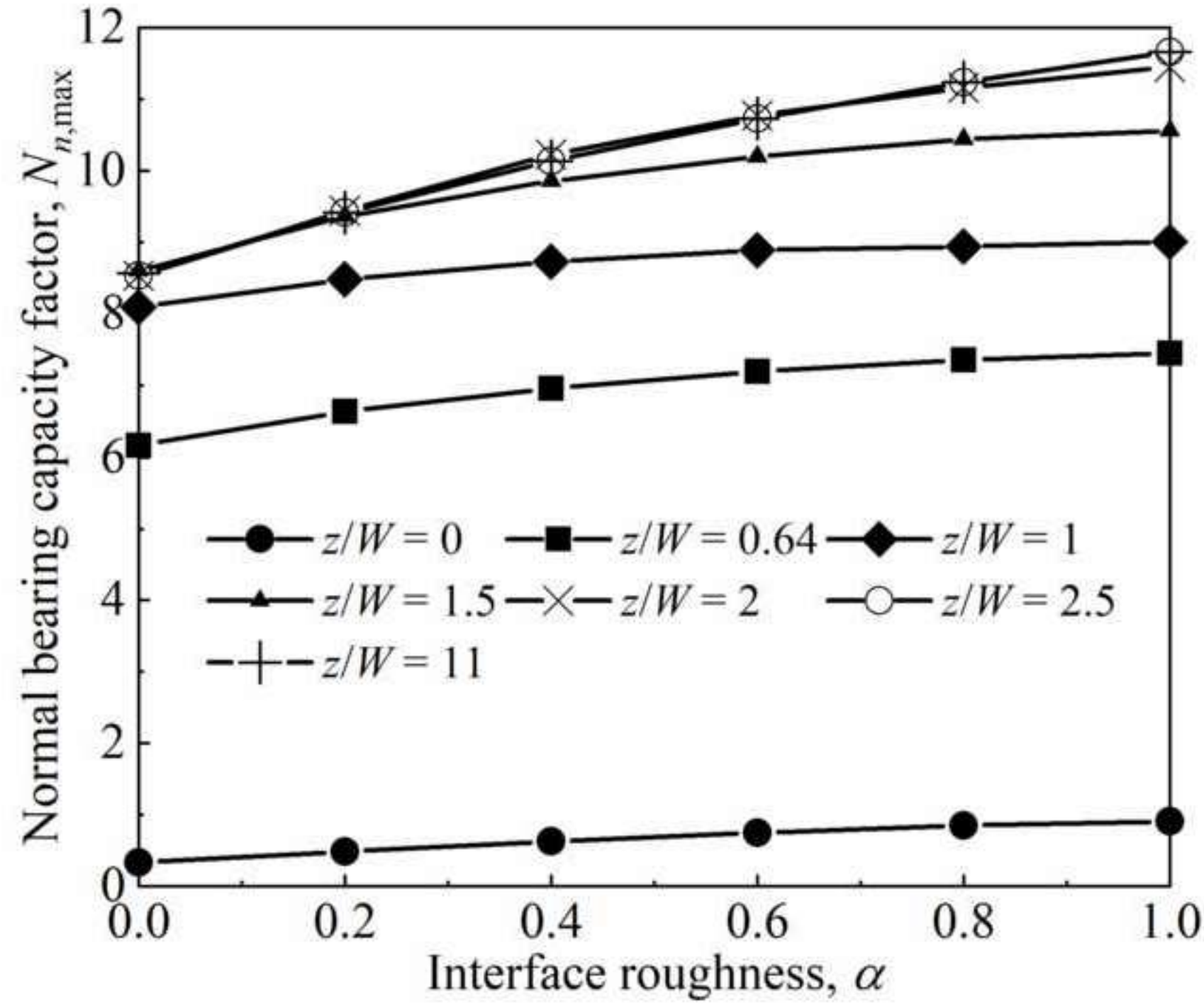


Figure9c

Click here to access/download;Figure;Fig9(c).tif

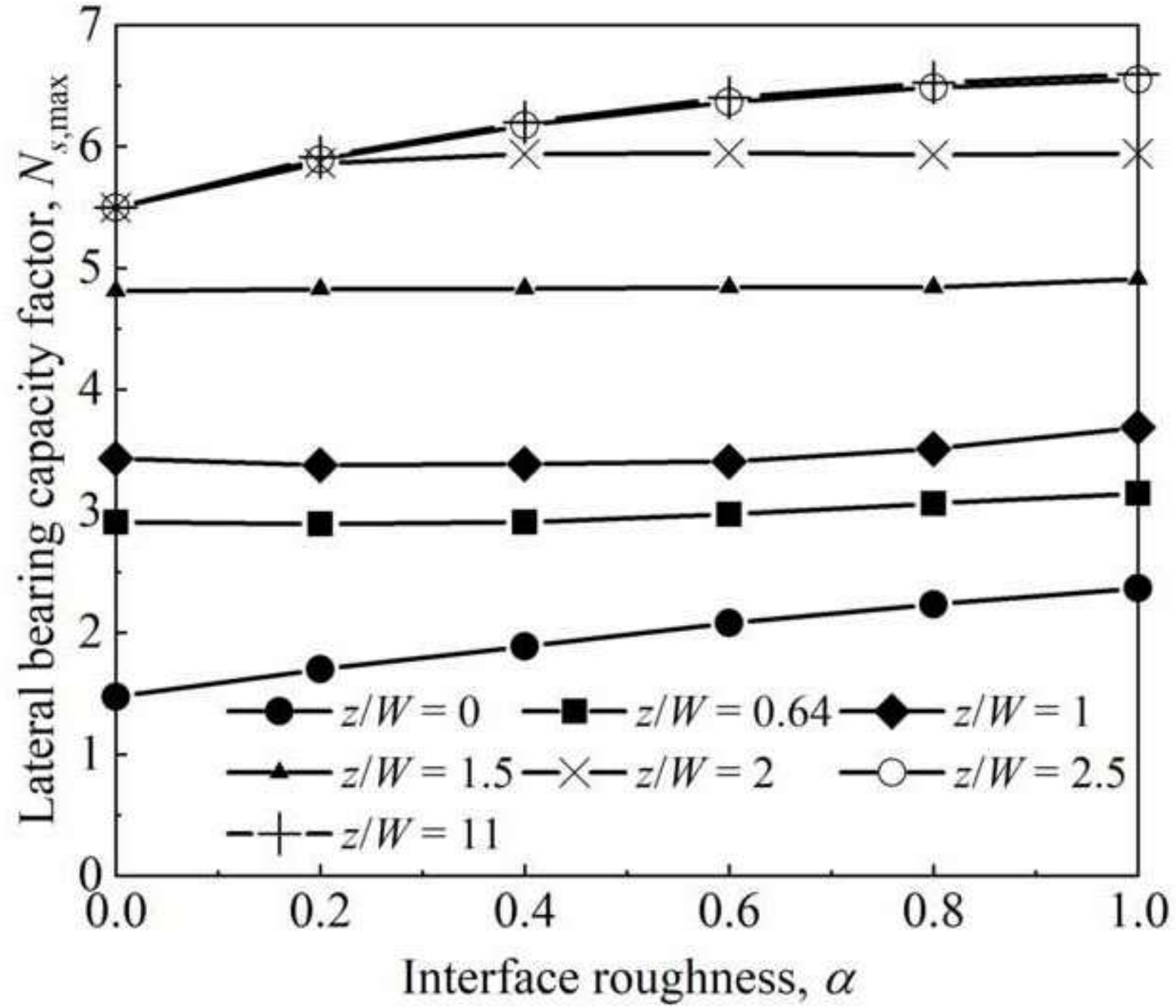


Figure9d

Click here to access/download;Figure;Fig9(d).tif

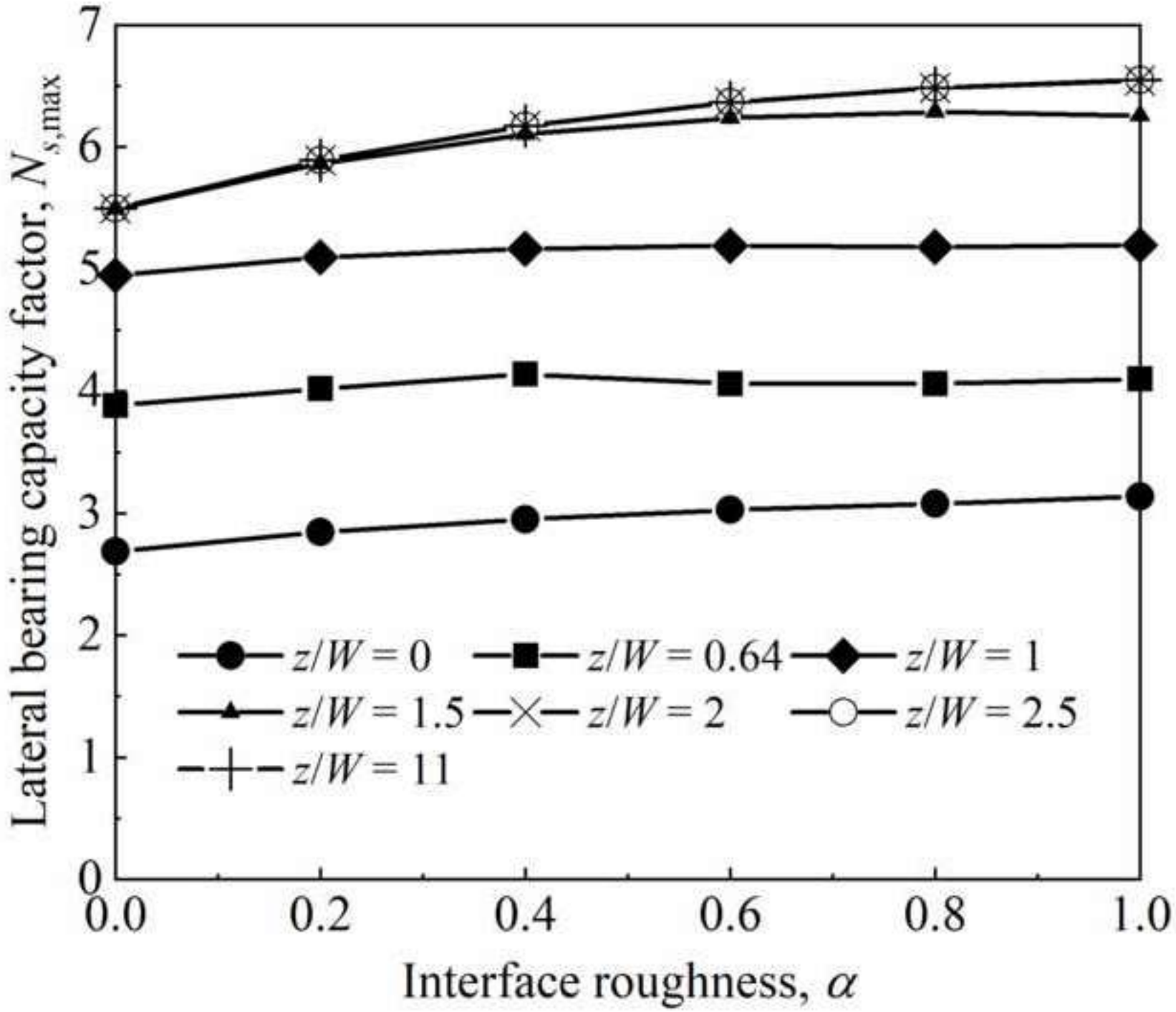


Figure9e

Click here to access/download;Figure;Fig9(e).tif

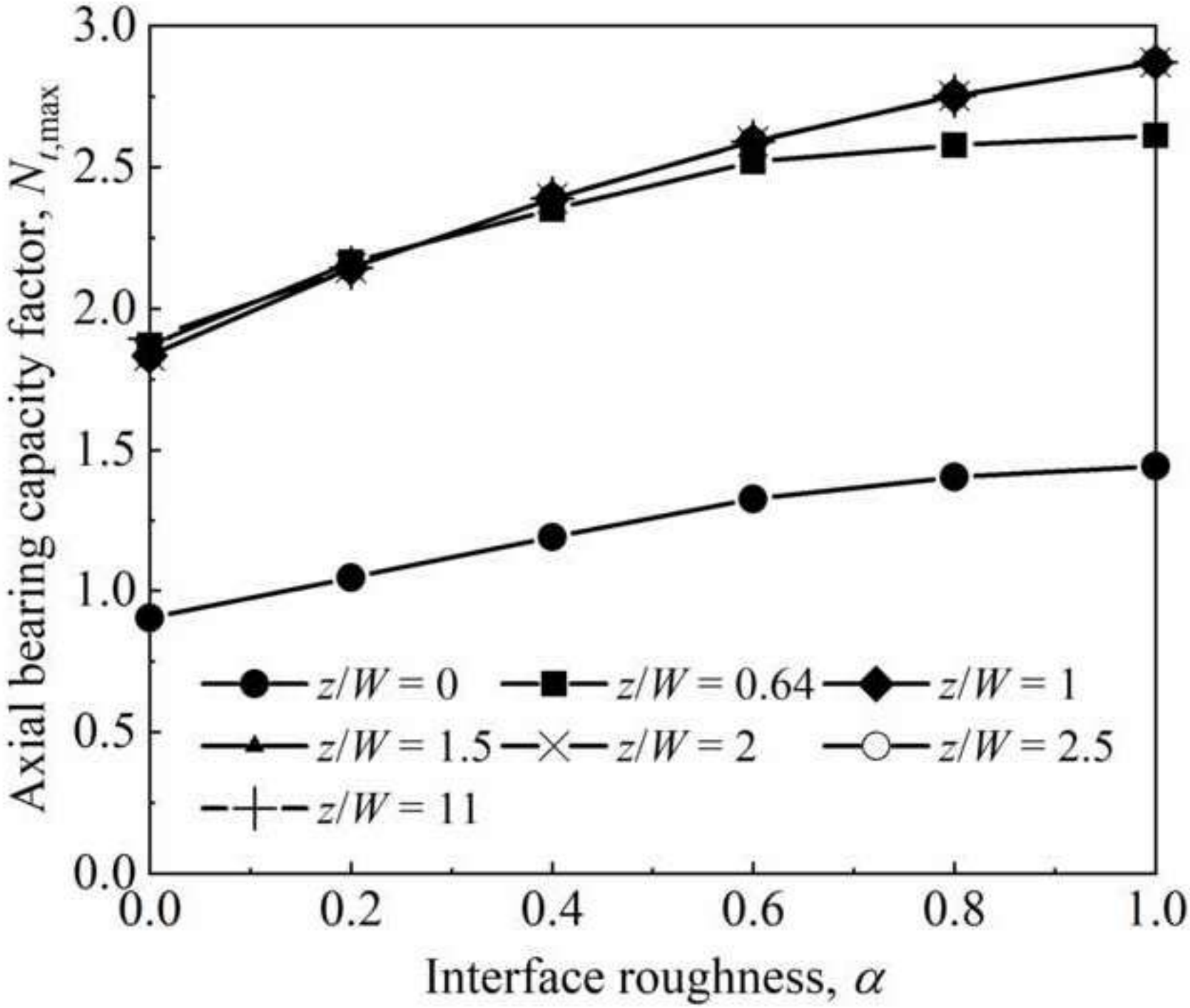
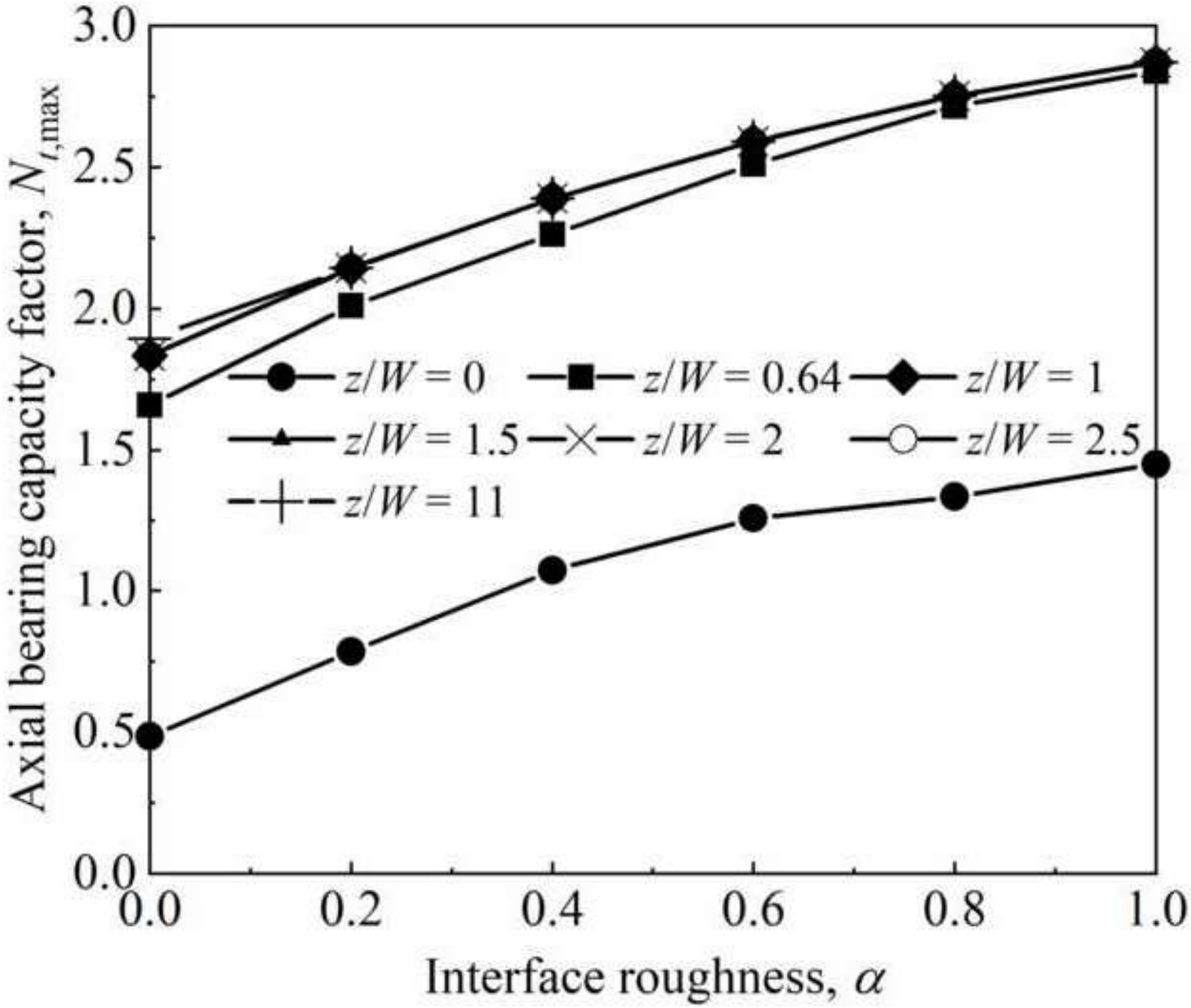
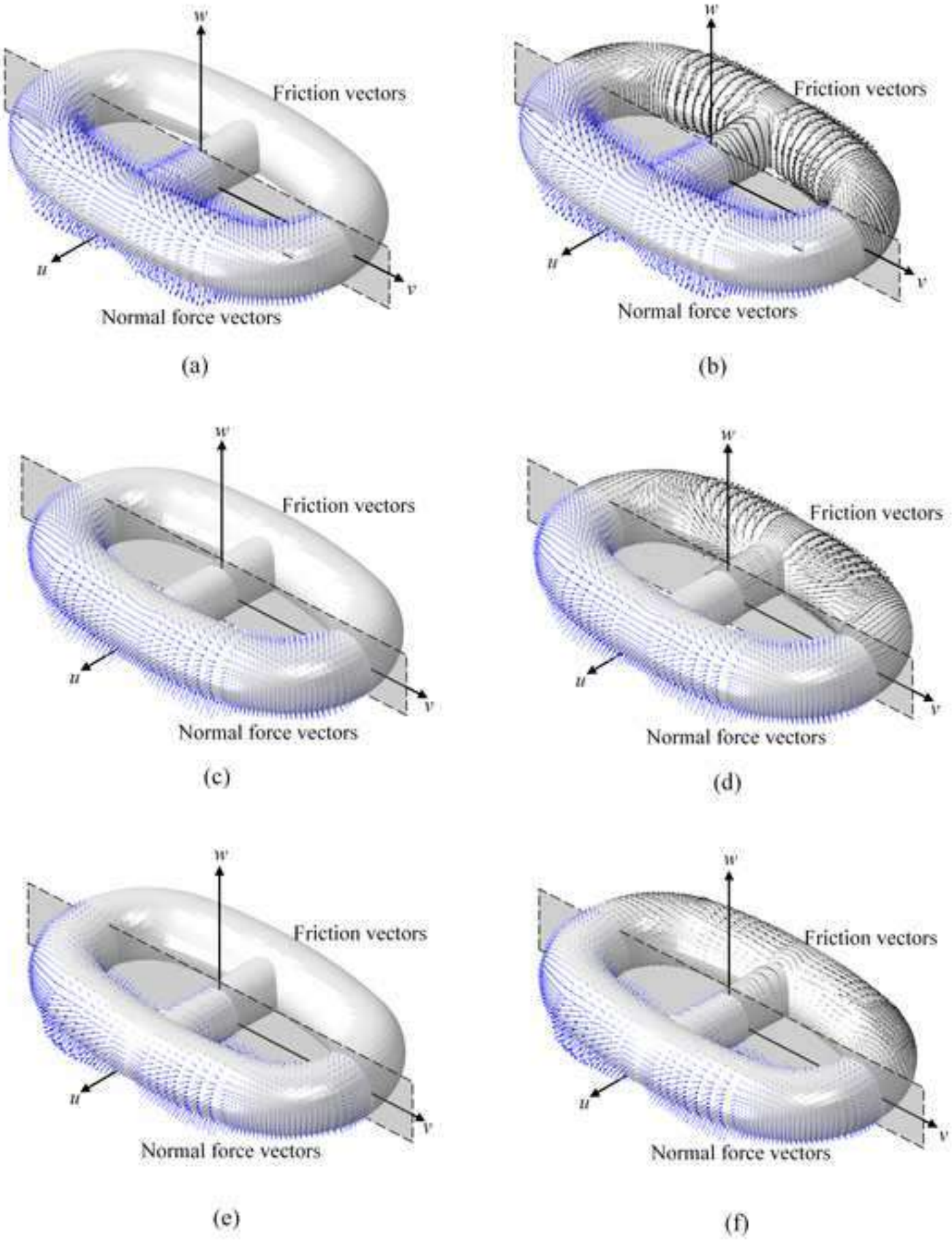


Figure9f

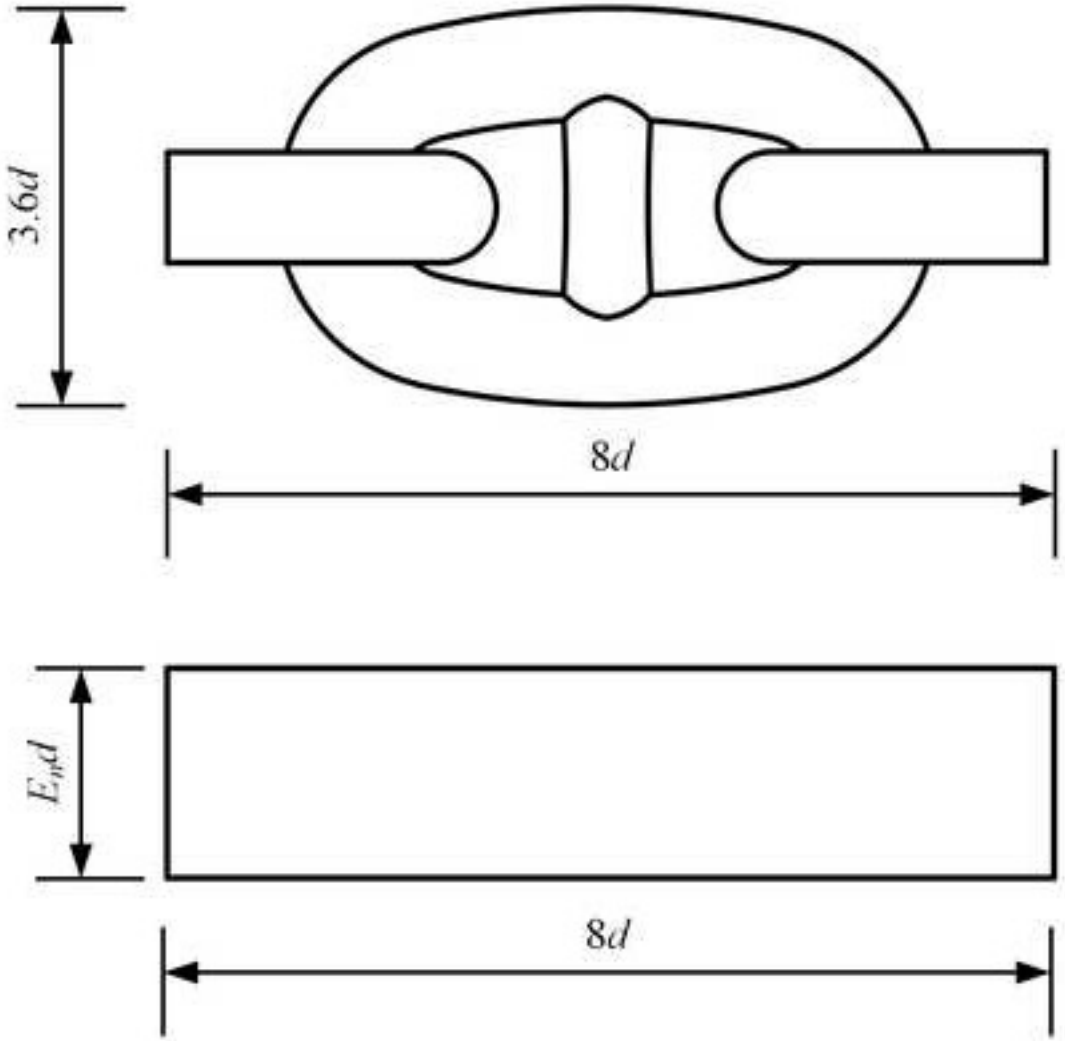
Click here to access/download;Figure;Fig9(f).tif



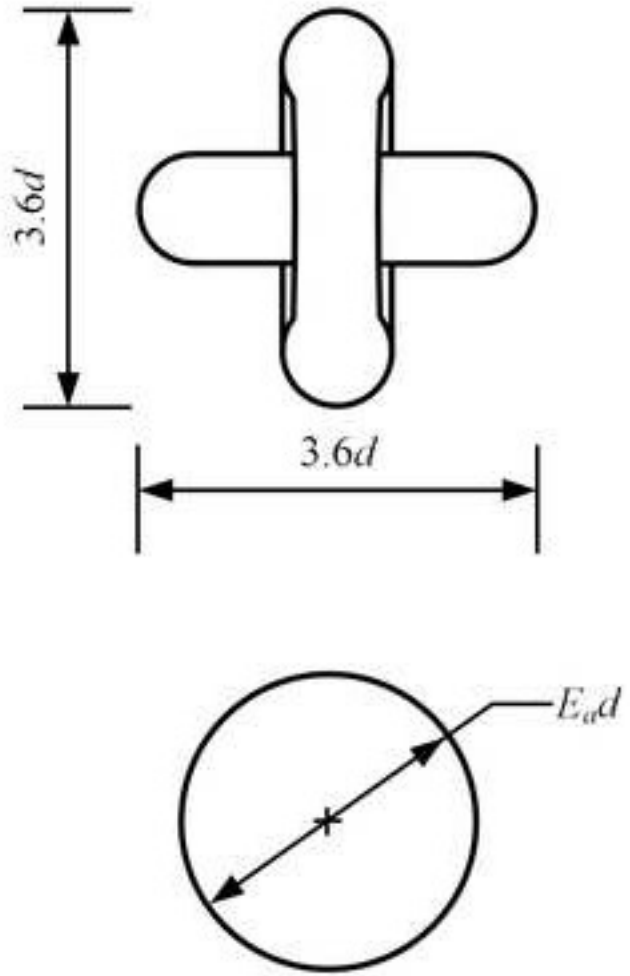
Click here to access/download;Figure;Fig10.tif



Click here to access/download;Figure;Fig11.tif



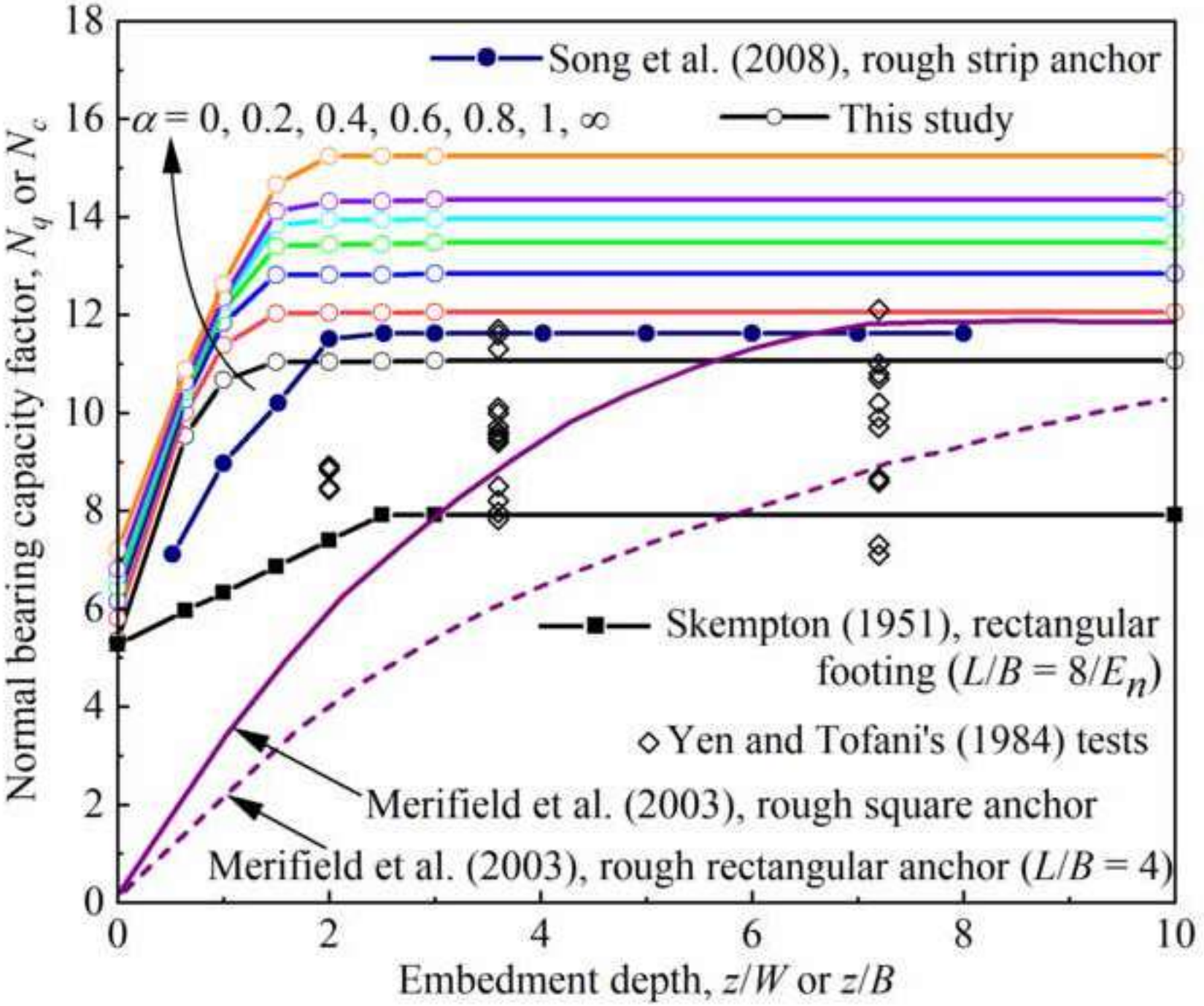
(a)



(b)

Figure12a

Click here to access/download;Figure;Fig12(a).tif



Click here to access/download;Figure;Fig12(b).tif

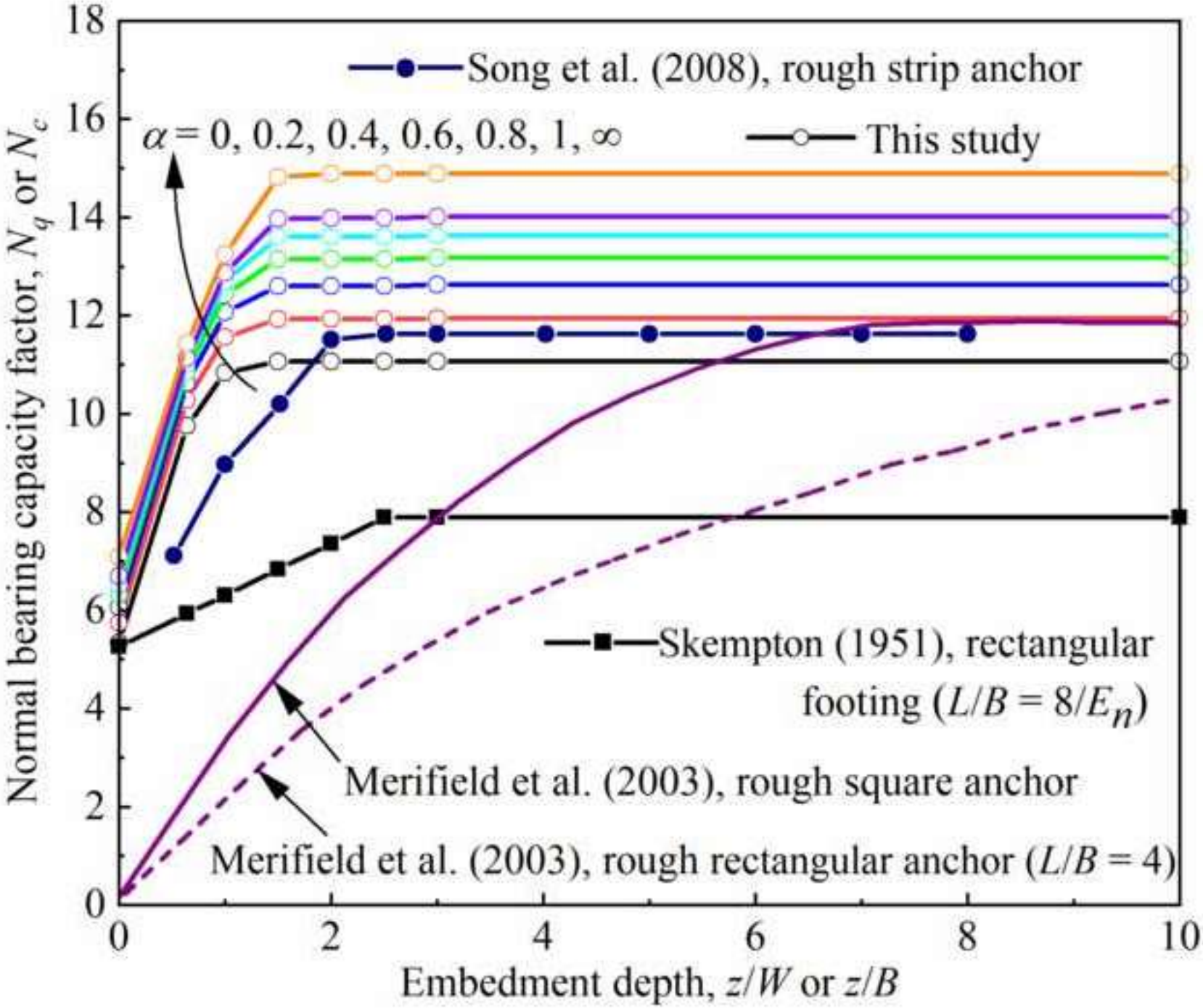


Figure12c

Click here to access/download;Figure;Fig12(c).tif

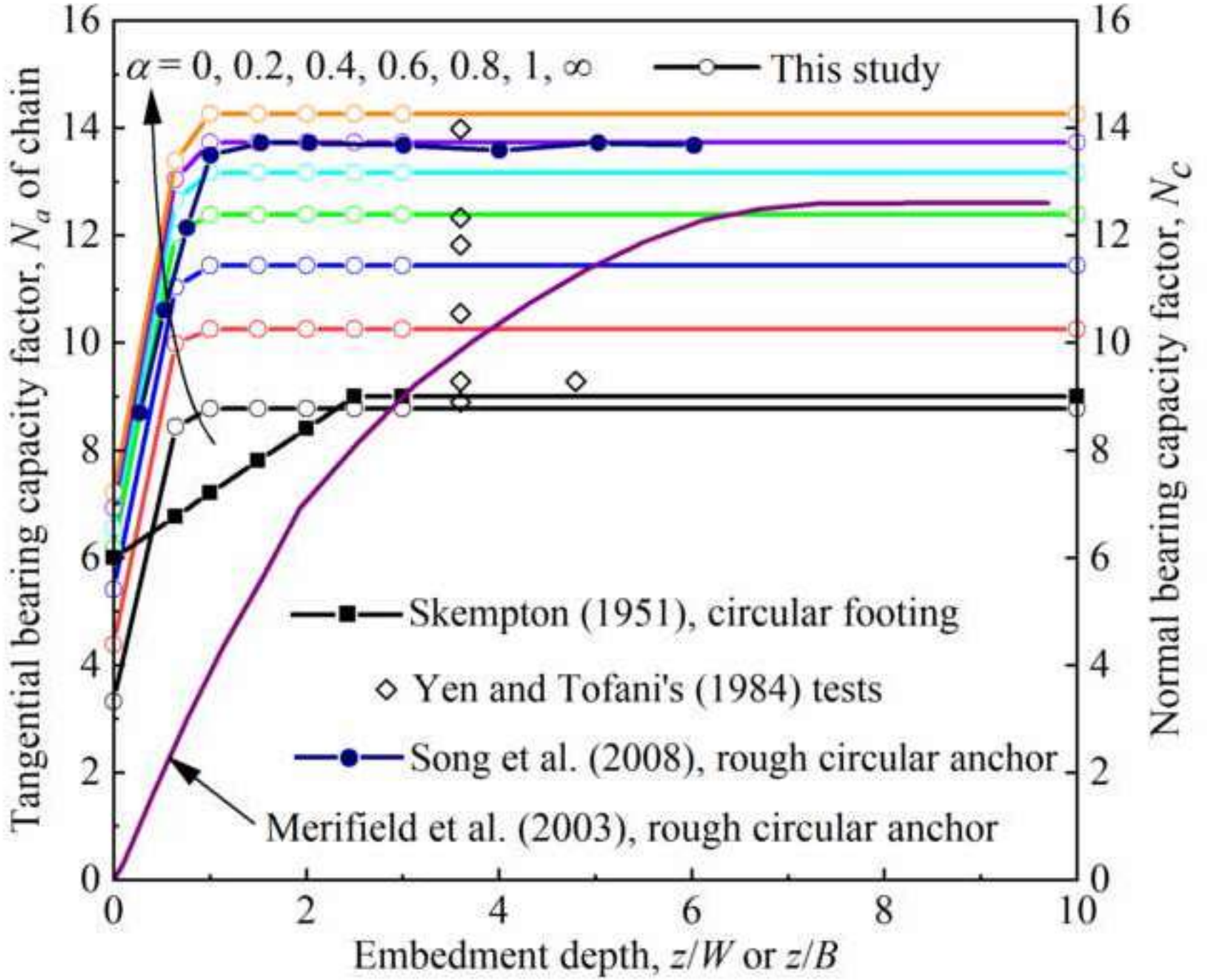


Figure12d

Click here to access/download;Figure;Fig12(d).tif

